

Geochimica et Cosmochimica Acta

JOURNAL OF THE GEOCHEMICAL SOCIETY
AND THE METEORITICAL SOCIETY

ISSN 0016-7037
Volume 124
January 1, 2014

EXECUTIVE EDITOR: MARK NORMAN

ARTICLES
EDITOR:

JEREMY C. ALY
YIM ANGLY
LAWRENCE M. ANSHUTZ
WOLFGANG BAER
MAYRA B. BATHURST
BRUNO S. BERNIERI
JOHN BURNETT
JEAN-FRANÇOIS BUREL
ANDREW ROSE BOWEN
MARTIN BRETHERTON
JAMES J. BROOKS
PETER BURROUGHS
BRUNO H. BURTON
ELIZABETH A. CARRILL
JEREMY G. CAVALLARO
TERRY CHAPMAN
JON CHAPMAN
GEORGE COHEN

NICOLAUS DUCHESNE
ANDREW DUCHESNE
JACQUES FLORENTIN
JEROME FLORENTIN
JENNIFER GAGNE
DAVID L. GARDNER
JENNIFER N. GARDNER
CRAIG M. HALL
PETER HALL
GREGORY P. HERRICK
EDWIN HERRICK
SANDRA HERRICK
THOMAS DELAUNAY
SILVIA MARIA DELAUNAY
ANDREW D. DELAUNAY
BRUNO DELAUNAY
KARIN DELAUNAY
CLAUD DELAUNAY

DAVID T. JENNINGS
CHRISTOPHER S. KYLE
PETER L. KYLE
CHRISTOPHER KYLE
S. KUMAR
ALEXANDER N. KYLE
TIMOTHY J. LLOYD
TOM MCCALLUM
JASON MCCORMICK
ANDREW MCCORMICK
JACK MONTAGNIER
JAMES W. MONTAGNIER
ANDREW MONTAGNIER
ALEXANDER MONTAGNIER
HAROLD MONTAGNIER
ALEXANDER MONTAGNIER
MARTIN MONTAGNIER
BRYAN MONTAGNIER

DANIELA PONTICORVO
CAROLINE L. PONTICORVO
AND PONTICORVO
GAIL S. PONTICORVO
MARK PONTICORVO
W. L. PONTICORVO
PETER W. PONTICORVO
JENNIFER M. PONTICORVO
CLAIRE PONTICORVO
YAN PONTICORVO
SARA S. PONTICORVO
NINA PONTICORVO
EUGENE A. PONTICORVO
AND PONTICORVO
SARA PONTICORVO
THOMAS J. PONTICORVO
MARTIN PONTICORVO
DANIEL L. PONTICORVO

JAMES S. PONTICORVO
CAROLINE L. PONTICORVO
AND PONTICORVO
GAIL S. PONTICORVO
MARK PONTICORVO
W. L. PONTICORVO
PETER W. PONTICORVO
JENNIFER M. PONTICORVO
CLAIRE PONTICORVO
YAN PONTICORVO
SARA S. PONTICORVO
NINA PONTICORVO
EUGENE A. PONTICORVO
AND PONTICORVO
SARA PONTICORVO
THOMAS J. PONTICORVO
MARTIN PONTICORVO
DANIEL L. PONTICORVO

Volume 124

Articles

- A. CARACASANO, D. BASSO, D. E. JACOB, D. STORZ, G. RIBONDI, F. BENZONI, E. DUTREUX: The covalline red alga *Lobophytum lachrymans* L. affinis as proxy of climate variability in the Yemen coast, Gulf of Aden (NW Indian Ocean) 1
- M. C. SORINA, M. A. VAN ZUILEN, P. PHILLIPOT: Structural characterization by Raman hyperspectral mapping of organic carbon in the 3.46-billion-year-old Apex chert, Western Australia 18
- J. YANG, J. I. GOLDBERG, E. R. D. SCOTT, J. R. MICHAEL, P. G. KOTULA, A. GRIMBERG, I. LEYA: Thermal and collisional history of Tishomingo from meteorite: More evidence for early disruption of differentiated planetesimals 34
- D. BESING, L. XIAO, L. HUANG, L. JIAN, Z. TIAN, Z. XIAO, L. JIAN, N. WU: Reduction of jarosite by *Shewanella oneidensis* MR-1 and secondary mineralization 54
- D. E. LAURIE, A. W. DALL, D. R. AGUIRRE, L. L. HERRICK, J. P. ANDERSON, P. REYNOLDS: Modelling microbial reaction rates in a submarine hydrothermal vent chimney wall 72
- F. GONZALEZ, V. K. SHARMA, M. PETTINE, L. CAMPANELLA, F. J. MILLER: Reduction of selenite by cysteine in ionic media 98
- C. HEUER, B. SHAFER, A. PANDOLFI: A new pore-scale model for linear and non-linear heterogeneous dissolution and precipitation 109
- J. ISA, A. E. ROBIN, J. T. WASSON: R-chondrite bulk-chemical compositions and diverse oxides: Implications for parent-body processes 131
- T. J. ZAGA, L. R. NYTLER, F. GYNGARD, C. M. O'D. ALEXANDER, R. M. STROUD, E. K. ZONNIK: A transmission electron microscopy study of presolar spinel 152
- S. SCOTT, I. GONKARSON, S. ANKORSSON, A. STEFANSSON: Gas chemistry, boiling and phase segregation in a geothermal system, Hellishell, Iceland 170

Continued on outside back cover



A large column analog experiment of stable isotope variations during reactive transport: I. A comprehensive model of sulfur cycling and $\delta^{34}\text{S}$ fractionation

Jennifer L. Druhan^{a,*}, Carl I. Steefel^b, Mark E. Conrad^b, Donald J. DePaolo^{a,b}

^a Department of Earth and Planetary Science, University of California Berkeley, Berkeley, CA 94720, United States

^b Earth Sciences Division, Lawrence Berkeley National Laboratory, Berkeley, CA 94720, United States

Received 6 March 2013; accepted in revised form 25 August 2013; available online 11 September 2013

Abstract

This study demonstrates a mechanistic incorporation of the stable isotopes of sulfur within the CrunchFlow reactive transport code to model the range of microbially-mediated redox processes affecting kinetic isotope fractionation. Previous numerical models of microbially mediated sulfate reduction using Monod-type rate expressions have lacked rigorous coupling of individual sulfur isotopologue rates, with the result that they cannot accurately simulate sulfur isotope fractionation over a wide range of substrate concentrations using a constant fractionation factor. Here, we derive a modified version of the dual-Monod or Michaelis–Menten formulation (Maggi and Riley, 2009, 2010) that successfully captures the behavior of the ^{32}S and ^{34}S isotopes over a broad range from high sulfate and organic carbon availability to substrate limitation using a constant fractionation factor. The new model developments are used to simulate a large-scale column study designed to replicate field scale conditions of an organic carbon (acetate) amended biostimulation experiment at the Old Rifle site in western Colorado. Results demonstrate an initial period of iron reduction that transitions to sulfate reduction, in agreement with field-scale behavior observed at the Old Rifle site. At the height of sulfate reduction, effluent sulfate concentrations decreased to 0.5 mM from an influent value of 8.8 mM over the 100 cm flow path, and thus were enriched in sulfate $\delta^{34}\text{S}$ from 6.3‰ to 39.5‰. The reactive transport model accurately reproduced the measured enrichment in $\delta^{34}\text{S}$ of both the reactant (sulfate) and product (sulfide) species of the reduction reaction using a single fractionation factor of 0.987 obtained independently from field-scale measurements. The model also accurately simulated the accumulation and $\delta^{34}\text{S}$ signature of solid phase elemental sulfur over the duration of the experiment, providing a new tool to predict the isotopic signatures associated with reduced mineral pools. To our knowledge, this is the first rigorous treatment of sulfur isotope fractionation subject to Monod kinetics in a mechanistic reactive transport model that considers the isotopic spatial distribution of both dissolved and solid phase sulfur species during microbially-mediated sulfate reduction.

© 2013 Elsevier Ltd. All rights reserved.

1. INTRODUCTION

Microbially mediated redox reactions are capable of generating large stable isotope fractionations and are a

principle cause of the wide range of $\delta^{34}\text{S}$ values observed in both marine and terrestrial sediments (Canfield, 2001). Dissimilatory sulfate reduction (DSR) may occur in any anaerobic environment where both sulfate and labile organic carbon are available, such as in marine sediments and poorly drained soils. As a result, DSR exerts a primary role in the global sulfur cycle. Though it occurs ubiquitously, DSR is a kinetically controlled process commonly characterized by sharp reactive gradients (e.g. Thamdrup et al.,

* Corresponding author. Address: 450 Serra Mall, Braun Hall, Building 320, Stanford University, Stanford, CA 94305, United States. Tel.: +1 520 730 6493.

E-mail address: jdruhan@stanford.edu (J.L. Druhan).

1994; Benner et al., 1999; Wijsman et al., 2001; Dale et al., 2008; Widerlund et al., 2012). A clear example of this dynamic behavior is demonstrated during amended subsurface biostimulation where the introduction of an exogenous organic carbon source leads to rapid microbial growth and reduction of available electron acceptors. Recent work at the Old Rifle site, a uranium contaminated aquifer in Western Colorado, USA, has shown substantial enrichment in sulfate $\delta^{34}\text{S}$ associated with the onset of sulfate reduction (Druhan et al., 2008, 2012). Here we present a large-scale column experiment designed to resolve both chemical and isotopic spatial and temporal gradients over a 1 m flow path amended by an organic carbon source (acetate) under conditions analogous to the Old Rifle field experiments. The datasets obtained from this study provide an unprecedented view of the highly dynamic region adjacent to an organic carbon point source and are interpreted through simulation of DSR and associated stable isotope fractionation in a new version of the CrunchFlow biogeochemical reactive transport model (Giambalyo et al., 2002; Steefel et al., 2003, 2005; Maher et al., 2006, 2009; Li et al., 2009, 2010, 2011; Navarre-Sitchler et al., 2011; Druhan et al., 2012, 2014).

It is the purpose of this paper to:

- (1) describe the design and results of the large-scale column experiment;
- (2) demonstrate incorporation of the stable isotopes of sulfur in a dual-Monod kinetic expression such that fractionation is accurately modeled at both high and low substrate availability;
- (3) verify accurate simulation of the chemical and isotopic gradients in reactant and product sulfur species using a kinetic fractionation factor obtained from field-scale analysis (Druhan et al., 2012);
- (4) utilize the model to predict the final $\delta^{34}\text{S}$ values of secondary sulfur minerals accumulated in the sediment over the course of the experiment.

The development of rigorous isotope-specific Monod-type rate expressions are presented here in application to sulfur cycling during amended biostimulation, but are readily applicable to a variety of stable isotope systems associated with both steady state and transient biogenic redox environments. In other words, the association of this model with a uranium remediation experiment does not limit its applicability to more general redox systems. Furthermore, the ability of this model treatment to predict the isotopic composition of secondary minerals accumulated as a result of fractionating processes (item 4) offers an important means of interpreting solid phase isotopic compositions and tracking long-term stability of precipitates.

1.1. Bioremediation at Old Rifle

The Old Rifle site in western Colorado is the former location of a uranium and vanadium ore processing facility that operated for 34 years. During this period a large volume of mill tailings were accumulated on the site, leading to a persistent elevation in the heavy-metal and radionu-

clide concentration of the sediment and groundwater (DOE, 1999, 2011). In 2002 the DOE Office of Science initiated a series of pilot scale uranium bioremediation experiments at the Old Rifle site. Fe(III)-(oxy)hydroxide minerals such as goethite and ferrihydrite occur in abundance at the site and in most near-surface environments and correspondingly so do native populations of iron-reducing microbes. This natural prevalence supports development of stimulated *in situ* bioremediation strategies using native iron reducers in heavy-metal contaminated groundwater systems (Lovley, 2000; Jørgensen, 2007). The purpose of the original Old Rifle experiments was to demonstrate and optimize *in situ* stimulation of native iron reducers to directly reduce uranium as the insoluble mineral uraninite (Anderson et al., 2003; Williams et al., 2011). The inherent difficulty lies in targeting growth of iron reducing microbes within the larger community.

Biostimulation of the Old Rifle aquifer with supplementary organic carbon leads to rapid growth of first iron (oxy)hydroxide reducers and subsequently sulfate reducers. The transition from iron to sulfate reduction as the predominant terminal electron accepting process (TEAP) marks a critical shift in the dynamics of uranium reduction. Both sulfate and iron reducers are capable of direct enzymatic reduction of U(VI) (Lovley et al., 1991; Lovley and Phillips, 1992; Holmes et al., 2002; Suzuki et al., 2004), though field observations from the original Old Rifle biostimulation experiments suggested the onset of DSR was accompanied by a partial decline in aqueous uranium removal rates (Anderson et al., 2003; Vrionis et al., 2005). However, more recent Old Rifle experiments have indicated the onset of DSR is associated with enhanced long-term stability of reduced uranium precipitates (Williams et al., 2011), potentially as a result of the ability of aqueous sulfide, mackinawite and pyrite to act as reducing agents for U(VI) (e.g. Wersin et al., 1994; Hua et al., 2006). Bargar et al. (2013) have most recently suggested microbes can play a role in the abiotic reduction of U(VI) by mackinawite through a concurrent biotic–abiotic pathway during the DSR phase of the Old Rifle experiments. Such complex coupling of uranium and sulfur cycling in anoxic environments underscores the utility of reactive transport models capable of simulation and prediction of DSR and associated $\delta^{34}\text{S}$ enrichment.

A typical well gallery for an acetate amendment experiment at Old Rifle occupies a footprint of 200 m², consisting of three rows of down-gradient monitoring wells at distances of 2.5, 5 and 8.5 m from the injection wells (Williams et al., 2011). Dispersivity is calculated based on inert tracer data collected over these distances, resulting in values of 0.4–0.95 m (Fang et al., 2009; Yabusaki et al., 2011). Recent field modeling studies have incorporated physical and chemical heterogeneities through the use of inverse modeling techniques to obtain permeability distributions from bromide tracer data (Li et al., 2010), and distributions of bioavailable Fe(III) within this heterogeneous structure (Li et al., 2011). Such studies ubiquitously show that the region immediately adjacent to the organic carbon source plays a dominant role in the biogeochemical reactivity and U reduction of the system (Fang et al., 2009; Li

et al., 2009, 2010, 2011; Yabusaki et al., 2011; Druhan et al., 2012). However, at the field site an inherent inability to obtain direct measurements within this highly reactive zone has limited model validation. A primary focus of the present work is the design and results of a column system capable of obtaining <20 cm sampling resolution in this highly reactive zone, and application of a reactive transport model to this spatiotemporal dataset.

1.2. Flow-through column studies

Through-flowing columns packed with porous media to represent subsurface systems have been extensively used in a variety of hydrogeochemical applications (e.g. Burris et al., 1996; White et al., 1999; Steefel et al., 2003). The advantages of these systems as proxies to field scale studies include improved control over physical and chemical parameters, ability to vary these parameters (e.g. flow rate) and observe system response in ways that would be impractical at the field scale, improved ability to monitor and sample the system and correspondingly better constraints on the initial and boundary conditions necessary to model the data. The primary disadvantage is that a column can never precisely reproduce the suite of factors contributing to field scale behavior, and is at best only an *ex situ* representation of a small section of the natural system. Therefore the results obtained from column studies are not necessarily expected to directly extrapolate to field scale behavior, but provide an analog in which to identify primary controls and test the response to variations in boundary conditions.

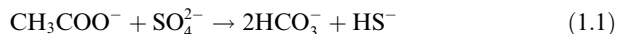
An obvious means of studying the highly reactive zone immediately adjacent to an organic carbon source during subsurface amendment is the construction of analog column experiments. Column-scale studies using sediment recovered from the Old Rifle aquifer have been applied to address reoxidation of uranium following the end of electron donor supplementation (Moon et al., 2007, 2009), effects of iron vs. sulfate reducing conditions on uranium sequestration (Komlos et al., 2008), and tracking of Fe(III) reduction using ^{57}Fe -labeled goethite (Moon et al., 2010). A column experiment using Old Rifle sediment and groundwater was used to identify the reaction network applicable to modeling field-scale bioremediation as part of the Li et al. (2009) study. To date no column study of Old Rifle conditions has employed multiple sampling points to verify simulation of transient reactive fronts developing in close proximity to the organic carbon source, and no column study has reported stable isotope fractionations associated with these chemical gradients.

1.3. Sulfur cycling and $\delta^{34}\text{S}$

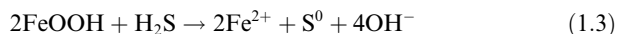
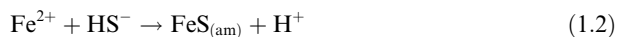
The reduction of sulfate to sulfide requires multiple bond breakages and electron transfers. As a result, equilibrium between sulfate and sulfide, as well as abiotic kinetic redox transformations between the two species, will not commonly proceed at ambient surface temperatures (Harrison and Thode, 1957). Biogenic reduction of the sulfate

anion, however, is extensively observed in near-surface anaerobic systems. This catalyzed reduction is commonly associated with fractionation of the stable isotopes of sulfur between the reactant and product species as a result of the differences in activation energy necessary to break the S–O bonds between the two isotopologues of sulfate. The characteristic fractionation of sulfur isotopes associated with bacterial sulfate reduction is commonly used to identify and even quantify bioactivity in subsurface environments (e.g. Habicht and Canfield, 2001; Massmann et al., 2003; Dale et al., 2009) and has specifically been utilized to analyze DSR due to biostimulation by multiple electron donor species (Knöller et al., 2006, 2008; Druhan et al., 2008, 2012). The maximum fractionation between ^{32}S and ^{34}S of residual sulfate and instantaneous product sulfide due to DSR is commonly reported as 46–47‰ (Harrison and Thode, 1958; Kaplan and Rittenberg, 1964), though recent pure culture experiments have shown even larger fractionations, up to 66‰, without evidence for disproportionation of intermediate species (Sim et al., 2011). The origin of these large fractionations is the four-step process originally described by Rees (1973) wherein sulfate is (1) transported through the cell membrane, (2) activated with adenosine-5'-triphosphate, (3) partially reduced to sulfite and ultimately (4) reduced and expelled from the cell interior as sulfide. Steps 1–3 are considered reversible and the combination of these processes, each with their own fractionation, results in the large and highly variable range of $\delta^{34}\text{S}$ values observed in natural systems (Brunner and Bernasconi, 2005). Therefore quantifying reduction rates based on measured $\delta^{34}\text{S}$, and similarly extending experimentally determined fractionation – rate relationships to field studies is complicated by a variety of additional influences (e.g. Stam et al., 2011). For example the type and availability of organic substrates (Habicht et al., 2005; Knöller et al., 2006) and the temperature of the system (Canfield et al., 2006) have been shown to influence fractionation of sulfur isotopes during sulfate reduction. As will be discussed further in Section 2, an additional complication arises when describing fractionation due to microbially catalyzed redox transitions such as sulfate and nitrate reduction, as these reactions are observed to follow Monod or Michaelis–Menten – type rate expressions (Rittmann and McCarty, 2001). Through the half-saturation term in these formulations, a shift from high to low substrate concentration can result in a transition in the order of the reaction (Jamieson-Hanes et al., 2012). If the rate expressions describing the behavior of individual isotopologues are not rigorously derived, such variable – order kinetics can lead to a discrepancy between the calculated fractionation factor and the ratio of the reactant and product isotopic compositions, i.e. the erroneous appearance of a variable fractionation factor. Such complexities between the physical and chemical conditions of the system and the simulation of isotopic fractionation motivate rigorous incorporation of the isotopes of biogenically mediated species into a multi-component, process based reactive transport model.

Sulfur cycling during acetate amendment at Old Rifle is driven by DSR as:



High background sulfate concentrations in the aquifer ranging from 8 to 11 mM (Williams et al., 2011; Druhan et al., 2012) support extensive sulfide production, which in turn directly precipitates with Fe^{2+} as amorphous FeS or mackinawite, as well as abiotically reduces iron oxide minerals to form elemental sulfur:



Previous studies have shown the sulfur isotope fractionation signal provides a precise indicator of DSR activity under Old Rifle conditions, and to date no indication of disproportionation pathways have been reported (Druhan et al., 2008, 2012). In particular the onset of sulfate reduction, which marks a critical transition in the uranium sequestration process, is more easily observed through the characteristic enrichment of $\delta^{34}\text{S}$ than variations in sulfur species concentrations because sulfate concentration measured in the field incorporates a large range in background variability, and the concentrations of sulfide and ferrous iron are impacted by mackinawite and elemental sulfur formation (Eqs. 1.2 and 1.3, Druhan et al., 2012). However, these studies have been limited to analysis of fluid samples collected from monitoring wells installed several meters down-gradient of the organic carbon source, resulting in only limited sulfide $\delta^{34}\text{S}$ measurements and no solid phase sulfur $\delta^{34}\text{S}$ values. Consequently, sulfur cycling and sulfur isotope fractionation modeled at the field site (Druhan et al., 2012) has never been extended to simulate the isotopic distributions of the reduced sulfur species. To our knowledge, this manuscript presents the first reactive transport model using an isotope-specific dual-Monod rate expression for sulfate reduction expanded to concurrently simulate the $\delta^{34}\text{S}$ distribution of all major dissolved and solid-phase sulfur species. The ability to simulate and predict mineralized sulfide $\delta^{34}\text{S}$ would provide a valuable tool to monitor long-term reduced species stability in the subsurface, and would present a substantial development in the treatment of stable isotopes in a reactive transport modeling framework.

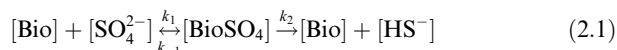
2. MODEL DEVELOPMENT

2.1. Monod kinetics

A variety of methods have been reported for modeling sulfur isotopes within a Monod-type rate expression in reactive transport studies (e.g. Jørgensen, 1979; Dale et al., 2009; Gibson et al., 2011; Druhan et al., 2012; Wehrmann et al., 2013). Gibson et al. (2011) simulated $\delta^{34}\text{S}$ enrichment of dissolved sulfate in good agreement with measured values in a series of column experiments where sulfate concentrations remained abundant relative to the half saturation constant. Disagreement between measured and simulated values at low sulfate concentrations were

suggested to occur as a result of diminished fractionation factors associated with limited sulfate availability. While true decreased kinetic fractionation factors are well documented under substrate limited conditions (Ingvorsen et al., 1984; Brunner and Bernasconi, 2005; Habicht et al., 2005), we will show in the following sections that modeling sulfur isotope fractionation using a Monod-type rate expression can also result in an erroneous, apparently variable fractionation factor as a result of the modeling treatment itself. For example, an apparent variation in the $\delta^{34}\text{S}$ fractionation factor has been reproduced through the use of a modeled biomass population that can grow and die out as substrates become limited (Druhan et al., 2012). Therefore, use of a single kinetic fractionation factor across a wide range of substrate concentrations cannot be demonstrated if the model lacks detailed consideration of the behavior of individual isotopes within the standard Monod-type rate expressions.

The relationship between the metabolically active, enzyme producing biomass and the electron donor and acceptor substrates is commonly described by a Michaelis–Menten (for enzyme kinetics) or Monod (for biomass growth) rate expression (Michaelis and Menten, 1913; Monod, 1942, 1949). A general form of the Monod rate law for microbial reduction of sulfate may be derived by assuming an intermediary biomass-substrate complex as (adapted from Roden, 2008):



where $[\text{Bio}]$ is the cell biomass, $[\text{SO}_4^{2-}]$ is the sulfate electron acceptor, $[\text{BioSO}_4]$ is the intermediary cell-substrate complex, $[\text{HS}^-]$ is the sulfide product species, and the k terms denote the individual rate constants of the reversible complexation and irreversible reduction reactions. It is important to note that Eq. 2.1 is a simplification of the 4-step dissimilatory sulfate reduction reaction mechanism described in Section 1.3. The rate of accumulation of the sulfide product species is then:

$$\frac{d[\text{HS}^-]}{dt} = k_2[\text{BioSO}_4] \quad (2.2)$$

The classic Monod rate expression makes two assumptions regarding metabolically active biomass. First, that the pool of cell-substrate complex is relatively small and rate constants are typically high, thus the concentration is considered as quasi-steady, resulting in an expression for biomass concentration as a function of the substrate, cell-substrate complex and rate constants:

$$[\text{Bio}] = \frac{k_{-1} + k_2}{k_1[\text{SO}_4^{2-}]} [\text{BioSO}_4] \quad (2.3)$$

Second, that the total biomass $[\text{Bio}]_T$ is defined as:

$$[\text{Bio}]_T = [\text{Bio}] + [\text{BioSO}_4] \quad (2.4)$$

Substituting Eq. 2.4 into Eq. 2.3 yields an expression for the cell-substrate complex as:

$$[\text{BioSO}_4] = \frac{[\text{Bio}]_T [\text{SO}_4^{2-}]}{[\text{SO}_4^{2-}] + \frac{k_{-1} + k_2}{k_1}} \quad (2.5)$$

Substituting Eq. 2.5 into the expression for the rate of product accumulation (Eq. 2.2) yields the general Monod rate law for sulfate reduction:

$$r = \frac{d[\text{HS}^-]}{dt} = \mu[\text{Bio}]_r \frac{[\text{SO}_4^{2-}]}{K_s + [\text{SO}_4^{2-}]} \quad (2.6)$$

where $\mu = k_2$ is the maximum specific growth rate and K_s is the half-saturation constant, calculated as (Koch, 1998; Roden, 2008):

$$K_s = \frac{k_{-1} + k_2}{k_1} \quad (2.7)$$

The rate law described above can be extended to treat systems in which more than one substrate is limiting and in which total biomass may vary (Rittmann and McCarty, 2001). Such a situation is commonly observed during biostimulation experiments in that the system is initially constrained by a deficit of labile organic carbon, but ultimately becomes limited by a depletion of available sulfate as carbon is artificially supplied in excess. This dual limitation is treated as a multiplicative rate law including individual species concentrations and half-saturation constants for acetate and sulfate as:

$$r_{\text{SRB}}^{\text{Ac}} = \mu_{\text{SRB}}^{\text{Ac}} [\text{Bio}]_{\text{SRB}} \left(\frac{[\text{SO}_4^{2-}]}{K_{\text{S-SRB}}^{\text{SO}_4^{2-}} + [\text{SO}_4^{2-}]} \right) \left(\frac{[\text{AC}]}{K_{\text{S-SRB}}^{\text{Ac}} + [\text{AC}]} \right) \quad (2.8)$$

where the overall rate for microbial sulfate reduction using acetate as an electron donor (r) is calculated using the maximum specific growth rate (μ), the biomass of sulfate reducing bacteria (Bio), and the individual activities and half-saturation constants (K) of sulfate $[\text{SO}_4^{2-}]$ and acetate $[\text{Ac}]$.

These Monod-type rate expressions are functions of the general form $x/(x+1)$. When substrate concentration is high, the value of $[\text{SO}_4^{2-}]$ is far greater than that of K_s and the corresponding microbial reduction rate is close to the maximum (μ). In this high-concentration regime, where $r \approx \mu$, the net rate is essentially zero order. However, as the concentration approaches and falls below the value of K_s , the rate law shifts to first-order behavior. As a result, the half-saturation constant governs the extent of substrate utilization at which this transition point occurs.

2.2. Behavior of stable isotopes

Modeling the individual isotopologues of any reactant subject to a Monod-type rate law ostensibly requires two or more equations of the form shown in Eq. 2.8 (e.g. Gibson et al., 2011; Jamieson-Hanes et al., 2012; Wehrmann et al., 2013). However, by definition this approach assumes that the kinetics of the two isotopologues are independent of one another. As we will now demonstrate, this assumption is not valid for all conditions of a rate expression that transitions through multiple reaction orders. First we define the observed fractionation factor (α_p) as the ratio of the rare to common isotope in the instantaneous product species

divided by the ratio of the isotopes in the reactant species (Mariotti et al., 1981; DePaolo, 2011):

$$\alpha_p = \frac{dP^*}{dP} \bigg/ \frac{N^*}{N} \quad (2.9)$$

where P (P^*) is the number of atoms or moles of the common (rare) isotope in the product species and N (N^*) is the number of atoms or moles in the common (rare) reactant species. Now we consider the case of a first order reaction involving both isotopologues, as in the case of the Monod-type rate expression when organic carbon or sulfate become limiting:

$$r = \frac{dN}{dt} = -\frac{dP}{dt} = -kN \quad (2.10a)$$

$$r^* = \frac{dN^*}{dt} = -\frac{dP^*}{dt} = -k^*N^* \quad (2.10b)$$

where r (r^*) is the rate of the reaction for the common (rare) isotopologue, and k (k^*) is the reaction rate constant of the common (rare) isotopologue. Combining expressions 2.9 and 2.10a and b the observed fractionation factor is then:

$$\alpha_p = \frac{k^*}{k} \quad (2.11)$$

This expression demonstrates, as required, that the isotopic fractionation factor is independent of the concentrations of the reactant and product species, and is a fixed value equal to the ratio of the rate constants.

Now we consider the case of a zero order reaction involving both isotopologues, as in the case of the Monod-type rate expression when both organic carbon and sulfate concentrations are substantially higher than the half-saturation constants:

$$r = \frac{dN}{dt} = -\frac{dP}{dt} = -k \quad (2.12a)$$

and

$$r^* = \frac{dN^*}{dt} = -\frac{dP^*}{dt} = -k^* \quad (2.12b)$$

In this zero order regime, combining equations 2.9 and 2.12a and b yields an observed fractionation factor calculated as:

$$\alpha_p = \frac{k^*}{k} \frac{N}{N^*} \quad (2.13)$$

This condition occurs when the sulfate reducing biomass (SRB) cells are saturated with sulfate, such that the total rate of reduction is fixed. For this situation, Eq. 2.13 suggests that the kinetics of the two isotopologues are not independent of one another. Furthermore, comparison of Eqs. 2.11 and 2.13 shows that for a single set of isotopic rate constants (k and k^*), the definition of α_p varies across reaction orders. This prediction is in clear disagreement with microbially mediated fractionation factors measured in both laboratory and field systems, and highlights an erroneous description of isotopic fractionation associated with the definition of zero order kinetics. Therefore, implementing Monod expressions as given in Eq. 2.8 for the individual

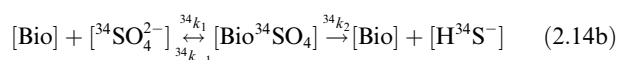
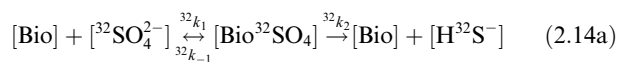
isotopes of sulfur in a model that transitions from high to low sulfate and organic carbon availability will result in inaccurate behavior. To overcome this issue we require a modified Monod expression capable of explicitly treating the relationship between the kinetics of the two isotopologues across a wide range of concentrations.

2.3. A modified dual-Monod rate expression for $\delta^{34}\text{S}$

The most direct means of circumventing the problems associated with the hyperbolic rate law when simulating individual isotopes is to assume first order kinetics (e.g. [Van Breukelen and Prommer, 2008](#)). Previous reactive transport models of sulfur isotope fractionation during DSR have assumed that the fractionation factor is always equal to the ratio of the rate constants, in other words a first order regime, despite the use of a hyperbolic rate expression ([Dale et al., 2009](#); [Wehrmann et al., 2013](#)). Alternatively one may attempt to restrict the system to either zero or first order conditions. This may be accomplished either within the experimental design or by altering the half-saturation constant in the model such that both the $^{32}\text{SO}_4^{2-}$ and $^{34}\text{SO}_4^{2-}$ concentrations are either substantially larger or smaller than K_S throughout the simulation. Field applications preclude the ability to restrict reactant concentrations and modifying half-saturation constants requires values that are inconsistent with those reported in the literature by several orders of magnitude ([Rittmann and McCarty, 2001](#); [Dale et al., 2008](#); [Fang et al., 2009](#)). In addition, the corresponding maximum specific growth rate (i.e. the rate constant) would no longer reflect an appropriate value for microbial redox processes.

We address this issue by making appropriate modifications to the Monod rate law to allow explicit treatment of individual stable isotopes. A similarly modified Monod rate expression for the microbially catalyzed reduction of nitrate isotopologues was derived by [Maggi and Riley \(2009, 2010\)](#). By deriving this isotope-specific hyperbolic rate function for sulfur isotopes we are generalizing the models used previously (e.g. [Dale et al., 2009](#); [Wehrmann et al., 2013](#)) such that the fractionation factor is functional across the full range of sulfate concentrations encompassing the half saturation constant.

Using the notation in Section 2.1, the two step reduction reaction for the isotopologues of sulfate are:



and the total biomass is then the sum of the free biomass and both isotopologue complexes:

$$[\text{Bio}]_T = [\text{Bio}] + [\text{Bio}^{32}\text{SO}_4] + [\text{Bio}^{34}\text{SO}_4] \quad (2.15)$$

This definition of the total biomass (Eq. 2.15) serves the important purpose of coupling the isotopologues through a common catalyzing microbial population. Under a quasi-steady state assumption for the total complexed biomass the resulting Monod expressions are then:

$$^{32}r = \frac{d[\text{H}^{32}\text{S}^-]}{dt} = ^{32}\mu[\text{Bio}]_T \frac{[^{32}\text{SO}_4^{2-}]}{[^{32}\text{SO}_4^{2-}] + ^{32}K_S \left(1 + \frac{[^{34}\text{SO}_4^{2-}]}{^{34}K_S}\right)} \quad (2.16a)$$

$$^{34}r = \frac{d[\text{H}^{34}\text{S}^-]}{dt} = ^{34}\mu[\text{Bio}]_T \frac{[^{34}\text{SO}_4^{2-}]}{[^{34}\text{SO}_4^{2-}] + ^{34}K_S \left(1 + \frac{[^{32}\text{SO}_4^{2-}]}{^{32}K_S}\right)} \quad (2.16b)$$

where $^{32}\mu$ ($^{34}\mu$) is equal to $^{32}k_2$ ($^{34}k_2$) and $^{32}K_S$ ($^{34}K_S$) is equal to $(^{32}k_{-1} + ^{32}k_2)/^{32}k_1$ ($(^{34}k_{-1} + ^{34}k_2)/^{34}k_1$). As a result the corresponding fractionation factor becomes:

$$\alpha_p = \frac{^{34}\mu}{^{32}\mu} \frac{^{32}K_S}{^{34}K_S} = \frac{^{34}k_2 \left(\frac{^{32}k_{-1} + ^{32}k_2}{^{32}k_1}\right)}{^{32}k_2 \left(\frac{^{34}k_{-1} + ^{34}k_2}{^{34}k_1}\right)} \quad (2.17)$$

Eq. 2.17 demonstrates that the coupled derivation yields a version of the Monod rate expression (Eq. 2.16a and b) that functions for the individual isotopologues and produces a constant fractionation factor independent of substrate concentration.

The Monod rate expression is formally derived for this quasi-steady state reaction involving a two-step, intermediary complex catalyzed by a single enzyme (Eq. 2.1). However, it has been shown that the same expression accurately describes a variety of more complex, multi-step and multi-catalyst processes and is capable of reproducing the observed rate even when the specific reaction mechanisms are unknown ([Van Cappellen and Gaillard, 1996](#)). As a result, the Monod expression is commonly used in reactive transport software to describe microbially catalyzed substrate utilization processes even when the pathways are more complex than Eq. 2.14a and b. As described in Section 1.3, microbial reduction of sulfate involves four intermediary steps, each with a unique fractionating process, which sum to the net apparent or observed fractionation ([Canfield, 2001](#); [Farquhar et al., 2003](#); [Johnston et al., 2005](#)). Commonly, the individual rate constants for each step are unknown, and simplification is required, as in the case of nitrate reduction studies modeled by [Maggi and Riley \(2009, 2010\)](#). In the present study, this is accomplished by assuming a single, common half-saturation constant (i.e. $^{32}K_S = ^{34}K_S$). This simplification effectively folds any difference in the true values of the isotopic half-saturation constants into the difference in rate constant (Eq. 2.17), such that the rate expressions implemented in CrunchFlow reduce to ([Druhan et al., 2012](#)):

$$^{32}r_{\text{SRB}}^{\text{Ac}} = ^{32}\mu_{\text{SRB}}^{\text{Ac}} [\text{Bio}]_{\text{SRB}} \left(\frac{[^{32}\text{SO}_4^{2-}]}{K_{\text{S-SRB}}^{\text{SO}_4} + [\text{SO}_4^{2-}]} \right) \left(\frac{[\text{Ac}]}{K_{\text{S-SRB}}^{\text{Ac}} + [\text{Ac}]} \right) \times \left(1 - \exp\left(\frac{\Delta G_r + m\Delta G_{\text{ATP}}}{\chi RT}\right) \right) \quad (2.18a)$$

$$^{34}r_{\text{SRB}}^{\text{Ac}} = ^{34}\mu_{\text{SRB}}^{\text{Ac}} [\text{Bio}]_{\text{SRB}} \left(\frac{[^{34}\text{SO}_4^{2-}]}{K_{\text{S-SRB}}^{\text{SO}_4} + [\text{SO}_4^{2-}]} \right) \left(\frac{[\text{Ac}]}{K_{\text{S-SRB}}^{\text{Ac}} + [\text{Ac}]} \right) \times \left(1 - \exp\left(\frac{\Delta G_r + m\Delta G_{\text{ATP}}}{\chi RT}\right) \right) \quad (2.18b)$$

where $^{34}\mu'$ indicates that any difference in the true ratio of $^{32}K_S$ and $^{34}K_S$ is folded into the rate constant. Thermody-

namic terms for the minimum free energy change of the reaction (ΔG_r), the minimum free energy change required for ATP synthesis (ΔG_{ATP}), the gas constant (R), and the absolute temperature (T) are also included to honor the free energy change required to drive the reaction and support ATP synthesis by restricting the reduction rate to proceed only above these minima (Jin and Bethke, 2003). Correspondingly the fractionation factor reduces to:

$$\alpha_p = \frac{{}^{34}\mu'}{{}^{32}\mu} \quad (2.19)$$

such that Eq. 2.19 is analogous to Eq. 2.11, though here the ratio of the rate constants ${}^{34}\mu'$ and ${}^{32}\mu$ is not simply equivalent to ${}^{34}k_2/{}^{32}k_2$ but includes differences in the isotope-specific values of k_1 , k_{-1} and k_2 (Eq. 2.17). Thus this section demonstrates that the total concentration of sulfate dictates the reaction order of the system (denominator of Eq. 2.18a and b), and within this regime the individual isotopes are not separable or independent of one another. Therefore a principle contribution of this study is a more generalized form of isotope-specific Monod-type rate expression that operates at both high and low substrate concentrations relative to the half saturation constant.

3. EXPERIMENTAL DESIGN AND METHODS

3.1. Column design

Sediments from a previously unamended section of the Old Rifle aquifer were trenched and extracted from beneath the saturated zone at a depth of ~ 4 m. After extraction they were immediately sieved to < 38 mm, sealed in opaque, gas-impermeable mylar bags and shipped to the University of California, Berkeley for storage at 4°C (Li et al., 2009). These sediments were subsequently wet packed into the column by adding small sections of solids along with artificial groundwater solution to keep the sediment entirely saturated without allowing the solids to settle through a substantial height of water and thus sort during packing. A total of 19.05 kg of sediment were used to fill the column.

Flow rate through the column was specified so as to match the average pore water velocity of $v = 50$ cm/day at the Old Rifle field site (Williams et al., 2011). With direct proportionality to the field scale flow rate, the 100 cm long column served as an analog to the first meter down gradient of the field site injection wells (Fig. 1). A diameter of 10 cm (cross-sectional area 78.5 cm^2) was selected to (1) provide a ratio of column diameter (D) to mean sediment grain diameter (d) larger than 40 so as to negate the effects of preferential flow along the walls on the mean radial flow distribution (Fand and Thinakaran, 1990) and (2) to provide adequate sample volume for $\delta^{34}\text{S}$ analysis of sulfide. Given an average porosity (ϕ) of 0.3 for Old Rifle sediments sieved and repacked in columns (Li et al., 2009), the pore volume is then $\sim 2350\text{ cm}^3$ and the Darcy flux of the column system is calculated as:

$$q = v\phi \quad (3.1)$$

yielding a value of $q = 15\text{ cm/day}$. For the specified cross sectional area the volumetric flux of the column is then

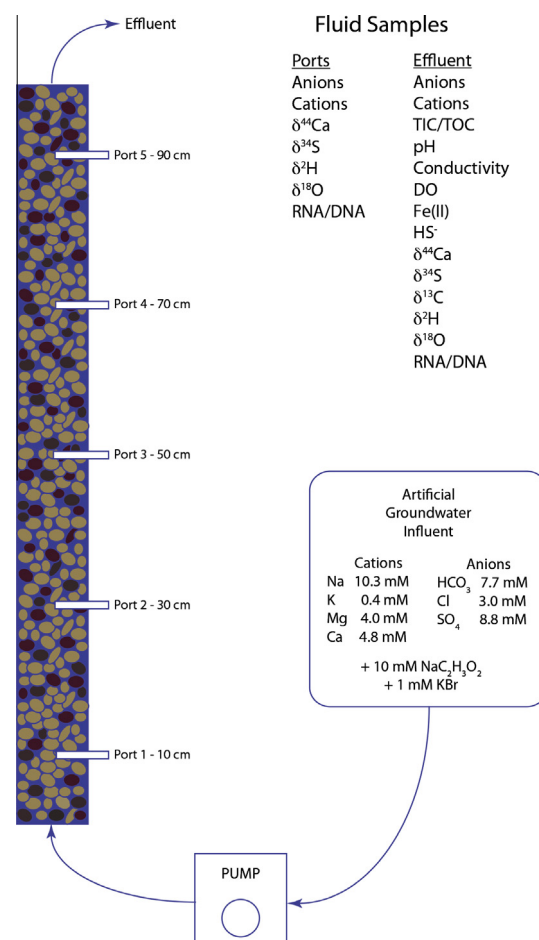


Fig. 1. Column schematic including influent artificial groundwater composition and a list of all fluid samples collected from the side ports and effluent.

$1178\text{ cm}^3/\text{day}$. A calibrated peristaltic pump operating between the influent reservoir and inlet of the column maintained this volumetric flux. At this volume, assuming 100% recovery, effluent collected for a full 24 h may be used to analyze $\delta^{34}\text{S}$ of sulfide in triplicate down to a concentration of $5\text{ }\mu\text{M}$.

Central to the column design are the use of side port samplers to obtain solute chemistry at a high spatial resolution. Bores were drilled into the side of the acrylic column wall at distances of 10, 30, 50, 70 and 90 cm from the base and the side ports were installed and secured with inert epoxy (Fig. 2a) such that the ceramic tubing extended 5 cm across the diameter of the column at each port (Fig. 2b). Consideration was given to the design of these samplers such that a flux-weighted average of the solution could be obtained at each location, rather than simply the fluid adjacent to the wall of the column. In order to accomplish this requirement, custom designed ports were fabricated (Soil Moisture Inc.) to consist of 6 cm long, 1 cm diameter porous ceramic tubes connected to plastic leurolock fittings (Fig. 2c). This ceramic is commonly used in lysimeters and combines both high porosity and permeability with a chemically inert composition.

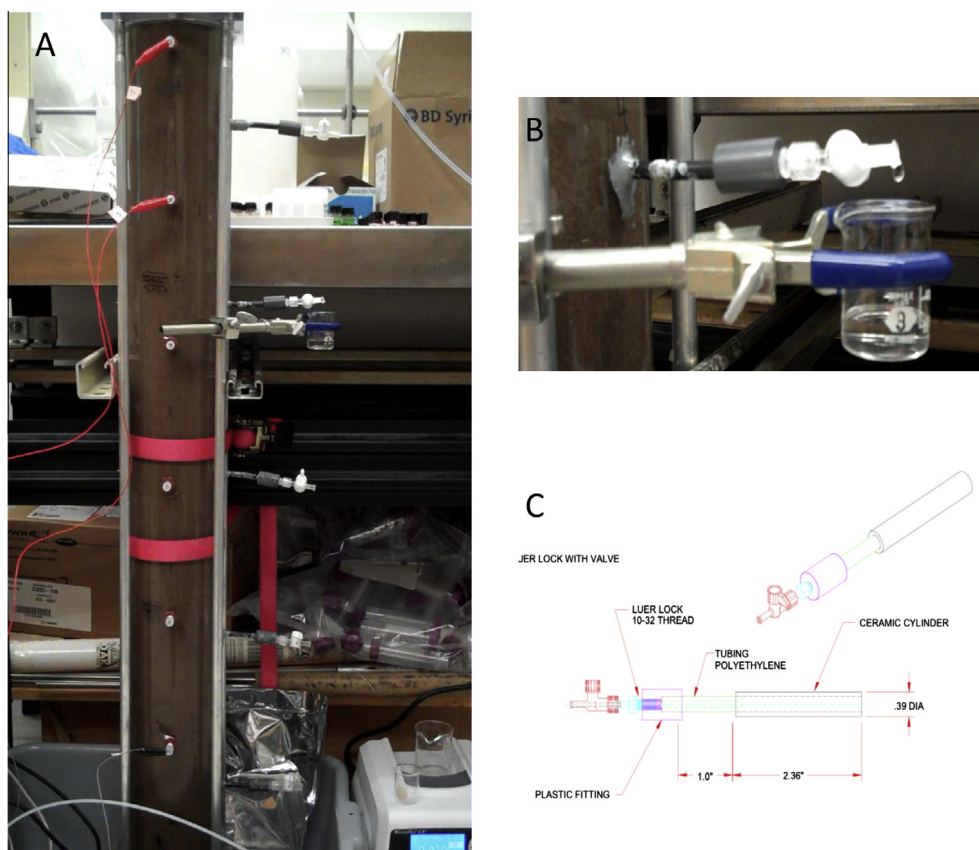


Fig. 2. (A) photograph of packed, through-flowing column, (B) close up of side port sampler installed through column wall during sample collection, (C) schematic of side port sampler.

Table 1

Concentration of salts added to DI water to achieve an artificial groundwater representing Old Rifle background conditions.

Species	Concentration (mol/L)
NaHCO ₃	7.70E–03
KCl	4.00E–04
MgSO ₄ ·7H ₂ O	4.00E–03
CaSO ₄	4.80E–03
NaCl	2.60E–03

3.2. Artificial groundwater

An artificial groundwater recipe was developed using the speciation code visual MINTEQ to match background well data from the Old Rifle aquifer (Williams et al., 2011). The solution (Table 1) was specified to saturation with respect to calcite and ordered dolomite at equilibrium with a 3.5:96.5 CO₂:N₂ gas headspace. The resulting charge balanced solution was mixed in 20 L batches and sparged with the 3.5:96.5 CO₂:N₂ gas (Praxair Co.) for 30 min per liter to achieve a final concentration of dissolved oxygen of <2 mg/L and a pH of 7.0. The solution was transferred without exposure to air to a sterile, 20 L gas-impermeable bag connected with Norprene tubing (Tygon Co.) to the bottom of the column via a peristaltic pump. Influent of this composition was driven continuously through the column for

116 days prior to the start of acetate amendment while flow rate, dissolved oxygen, pH, conductivity, anions and cations were monitored to verify stabilization of effluent values. Following this stabilization period, 50 L of the artificial groundwater solution were mixed and sparged with an additional 41.475 g of sodium acetate and 5.95 g of potassium bromide. This solution resulted in a final concentration of 9.75 mmol/L acetate and 1.32 mmol/L bromide. The total volume was stored in a 50 L inert, gas impermeable bag with a 3.5:96.5 CO₂:N₂ headspace and subsequently transferred in 10–20 L aliquots to smaller bags for delivery to the column. This process allowed introduction of multiple inert tracers in addition to the continuous bromide delivery in order to track flow field evolution during the electron donor amendment. Over the 43 days acetate was continuously supplied to the influent of the column, tracer breakthroughs were obtained on days 1, 24 and 40.

3.3. Aqueous sampling methods and analysis

Samples were collected daily from the five side ports and the effluent for anions, cations, and stable isotopes of hydrogen, oxygen, sulfur and calcium. Weekly samples were also collected for planktonic phase DNA (Druhan et al., 2014 companion paper). Additional samples were collected daily from the effluent only for total inorganic carbon and

organic carbon (TIC/TOC), $\delta^{13}\text{C}$, pH, conductivity, dissolved oxygen (DO), Fe(II), sulfide concentration and $\delta^{34}\text{S}$, and weekly for dissolved methane. The decision to limit atmospherically reactive samples such as inorganic carbon and sulfide to the effluent was made in order to accommodate a passive method of side port sampling that minimized disruption to the flow field. Fluid from side port samplers was obtained by clamping the column effluent tubing closed while keeping the influent peristaltic pump operating and opening a Luer lock™ fitting on a chosen side port. As a result fluid was driven from the base of the column to the height of the side port and discharged passively into a collection vial (Fig. 2b), while the saturated section of column above this height was held static by the back pressure of the closed effluent tubing. This method eliminated the need to apply suction to the side ports in order to obtain samples and thus provided a more representative measure of flux-weighted fluid chemistry at each location. Side port fluid was purged for 10 mL before sample was collected and preserved for individual analyses. Carbon chemistry and microbiology methodology and results are presented in a companion paper (Druhan et al., 2014 companion paper). The current manuscript details methods pertinent to sulfur speciation and $\delta^{34}\text{S}$ analysis, and all relevant data are reported in Appendices A–D.

Effluent samples sensitive to atmospheric exchange were collected by connecting the end of the effluent tubing to a degassed 50 mL glass syringe with a low-friction plunger. Samples for Fe^{2+} , sulfide and dissolved oxygen were collected in the glass syringe and immediately analyzed using a Hach DR2500 spectrophotometer with a photoilluminator using methods 8146, 8131 and 8316, respectively (Hach Company, Loveland, CO). Anion samples were collected and filtered directly into 0.5 mL auto sampler vials for analysis on a Dionex DX120 ion chromatograph. Cations were filtered and acidified with trace metal grade 12N HNO_3 for later analysis on a Perkin Elmer SCIEX Elan DRC II quadrupole ICP-MS with a dynamic reaction cell (DRC) using ammonia as a reaction gas to remove polyatomic interferences. Hydrogen and oxygen isotopes were filtered into 5 mL glass vials with septa caps and analyzed at the Laboratory for Environmental and Sedimentary Isotope Geochemistry at the University of California, Berkeley using a GV Isoprime isotope ratio mass spectrometer. Hydrogen measurements were made by coupling the Isoprime to a Eurovector Elemental Analyzer (EuroEA3028-HT) and oxygen measurements were made using a Liquid Autosampler (EuroAS300).

Sulfate $\delta^{34}\text{S}$ samples were collected daily from each of the five side ports and effluent of the column. Fluid samples were immediately pushed through 0.2 μM PTFE filters into vials containing BaCl_2 in 3 \times excess of influent sulfate concentrations to precipitate all aqueous sulfate as BaSO_4 . Sulfide samples were collected overnight by allowing column effluent to discharge directly into a 1L vial containing excess zinc acetate to precipitate ZnS (Carmody et al., 1998). Preserved ZnS precipitate was subsequently separated from solution and reprecipitated as Ag_2S for analysis. Sulfur isotopes were measured at the University of California, Berkeley, Laboratory for Environmental

and Sedimentary Isotope Geochemistry using a Eurovector model 3028 elemental analyzer in helium continuous flow mode interfaced with a GV Isoprime isotope ratio mass spectrometer. Long-term precision for the instrument is $\pm 0.15\text{‰}$ based on reference standard NBS-127 and in house standards. V_2O_5 was added to the BaSO_4 samples during loading as a combustion aid, yielding improvements on the reported precision. Sulfur isotope ratios are reported in standard delta notation relative to the Canyon Diablo Troilite standard as:

$$\delta^{34}\text{S} = \left(\frac{R_{\text{sample}}}{R_{\text{std}}} - 1 \right) \times 1000\text{‰} \quad (3.2)$$

where $R = {}^{34}\text{S}/{}^{32}\text{S}$. The difference in measured $\delta^{34}\text{S}$ values of aqueous sulfate and sulfide are reported as:

$$\varepsilon_{\text{meas}} = \delta^{34}\text{S}_{\text{SO}_4^{2-}} - \delta^{34}\text{S}_{\text{HS}^-} \quad (3.3)$$

3.4. Solid phase sampling methods and analysis

Following completion of the 43-day acetate amendment, flow was discontinued and the column was immediately placed in a portable glove bag under 5:95 $\text{CO}_2:\text{N}_2$ gas headspace at slight overpressure. Within the glove bag, sections of the column wall were drilled out at distances of 10, 30, 50, 70 and 90 cm from the base, consistent with the location of the side port samplers. Sediment was extracted from these locations and sealed in double layer mylar bags with oxygen scrubbers and stored at 4 °C. These samples were subsequently transferred to an anaerobic chamber where they were opened and allowed to dry in a 5:95 $\text{CO}_2:\text{N}_2$ atmosphere. Despite these precautions it was observed that the black coloration of the sediment acquired within the column during sulfate reduction was lost during the extraction process, potentially indicating reoxidation of FeS precipitates. As a result solid phase sulfur analysis was focused on quantitative recovery of elemental sulfur (Eq. 1.3) for both weight percent and $\delta^{34}\text{S}$.

Solid phase elemental sulfur extraction was accomplished by suspending 5 g bulk sediment in 25 mL of HPLC grade acetone following the methods described in Williams et al. (2011). After extraction, filtered aliquots of the acetone solutions were dried down and rinsed to obtain residual solids for $\delta^{34}\text{S}$ analysis following the methods described in Section 3.3. The remainders of the 0.2 μm filtered solutions were used to obtain the weight% of elemental sulfur in the bulk solid phase samples by analysis on a Perkin Elmer Series 200 high performance liquid chromatography (HPLC) system on a C18 reverse-phase HPLC column with a UV-vis Detector operating at 254 nm and an eluent of 95:5 methanol:water.

4. EXPERIMENTAL RESULTS AND DISCUSSION

4.1. Flow parameters

Bromide tracer data confirmed continuous delivery of artificial groundwater solution throughout the column for the 43 days of amendment (Fig. 3A). A deuterated water isotope spike was also introduced to the column on day 1

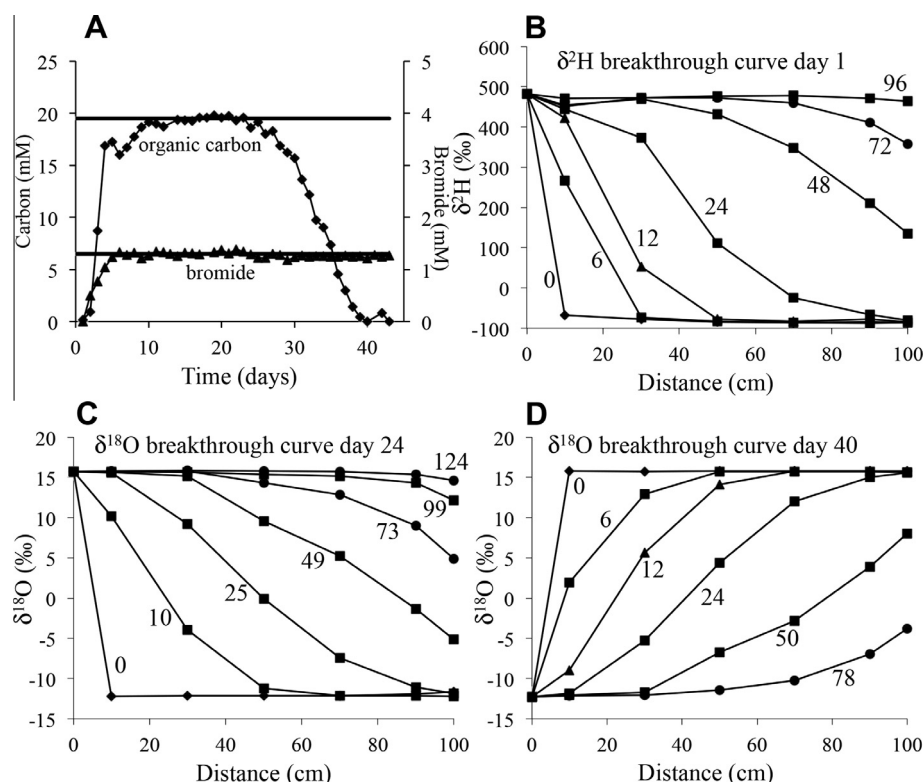


Fig. 3. (A) Organic carbon (acetate) and bromide concentrations in influent (horizontal lines) and effluent throughout the 43 day amendment, (B–D) deuterium and $\delta^{18}\text{O}$ tracer breakthrough curves started on days 1, 24 and 40, respectively. Individual curves are labeled by the hour since the start of tracer addition and are measured across the length of the column using influent, side port and effluent samples. All measurement errors are less than the size of the plotted data points (Section 3.3).

(Fig. 3B) and $\delta^{18}\text{O}$ tracers were introduced on days 24 (Fig. 3C) and 40 (Fig. 3D). For each day of the experiment, a Darcy flux was obtained by weighing a quantity of effluent fluid collected over a known period of time and dividing by the cross-sectional area of the column, assuming a fluid density of 1 g/cm^3 . Based on these data, porosity was calculated (Eq. 3.1) using pore water velocities corresponding to $C/C_0 = 0.5$ for each of the breakthrough curves shown. The 24-h profile was chosen for each analysis based on the distribution of tracer concentration across the column at this sampling time. Results (Table 2) show that the deuterium tracer introduced on day 1 yielded a porosity of 0.33, which is consistent with previous estimates of Old Rifle sediments recovered and packed into columns (Moon et al., 2007; Li et al., 2009). The $\delta^{18}\text{O}$ tracer pulses introduced as the acetate amendment experiment progressed show a slight increase in the pore water velocity in correspondence with a drop in the Darcy flux rate despite a constant pressure

applied by the pump to the inlet section of the column. The resulting calculated porosity indicates a decline of roughly 6% relative to the starting value in association with acetate augmentation. A falling head measurement conducted prior to the start of acetate addition yielded a permeability value of $1.08 \times 10^{-8} \text{ cm}^2$. Additional falling head measurements were omitted in order to preserve anaerobic conditions in the system.

The tracer data were also used to determine a longitudinal dispersion coefficient for the system, using the pore water velocities and breakthrough times obtained from the 24-h tracer profiles (Eq. 4.1). Here the dispersion coefficient is calculated as a function of

$$\frac{C}{C_0} = \frac{1}{2} \left[\text{erfc} \left(\frac{l - vt}{2\sqrt{Dt}} \right) + \exp \left(\frac{v}{D} \right) \text{erfc} \left(\frac{l + vt}{2\sqrt{Dt}} \right) \right] \quad (4.1)$$

the average pore water velocity (v), the distance along the flow path (l), and the time (t) at which the chosen C/C_0

Table 2

Tracer breakthrough curve analysis of pore water velocity and porosity for multiple inert tracers introduced over the course of the acetate amendment experiment.

Day	Tracer	Darcy flux (cm/min)	Pore water velocity at 24 h (cm/min)	Porosity
1	$\delta^2\text{H}$	$1.0\text{E}-02$	$3.00\text{E}-02$	0.33
24	$\delta^{18}\text{O}$	$8.5\text{E}-03$	$3.07\text{E}-02$	0.28
40	$\delta^{18}\text{O}$	$8.4\text{E}-03$	$3.10\text{E}-02$	0.27

occurs (Freeze and Cherry, 1979). The resulting dispersion coefficient of $0.2 \text{ cm}^2/\text{min}$ yields a dispersivity of roughly 7 cm for the given average pore water velocity. This dispersivity is substantially lower than the 0.4–0.95 m value obtained from field scale tracers and is attributed to decreased grain size distribution and removal of hierarchical heterogeneity effects in the sieved and repacked sediments (Gelhar et al., 1992).

4.2. Sulfur species concentrations

The concentrations of acetate and sulfate in the effluent of the column closely track one another as a result of the 1:1 molar ratio of electron donor and acceptor species required to drive sulfate reduction (Fig. 4A). Based on these effluent concentrations, sulfate reduction appears to have become the dominant TEAP roughly 23 days after the start of acetate addition. Acetate was supplied in excess of influent sulfate concentration with the intent of promoting complete reduction of the bioavailable sulfate pool, however, the effluent solute composition clearly demonstrates that acetate became the limiting nutrient at late time. By day 40, effluent acetate concentration (measured as TOC) was not detectable, while effluent sulfate correspondingly stabi-

lized at roughly 0.5 mM. This result indicates that multiple pathways of acetate utilization in addition to catabolic sulfate reduction were active. Such processes may include Fe(III) reduction by microbial metabolism, which can be hard to detect because of the rapid precipitation of FeS, and anabolic pathways supporting growth of the active microbial populations. The relative importance of these influences will be tested in the subsequent sections by incorporation in the multi-component reactive transport model.

Fluid samples obtained from side ports provide 10–20 cm sampling resolution along the length of the column. Sulfate concentrations obtained from these locations illustrate the spatiotemporal development of the sulfate reduction gradient (Fig. 4B). Between days 25–30 the removal of sulfate from solution appears to occur uniformly across the length of the column, as would be anticipated by a fixed (zero order) reduction rate. However, after roughly day 30, the majority of total sulfate reduction occurring on any given day takes place predominantly in the first 70 cm of the column, reflecting a higher-order reduction rate. This trend becomes more pronounced with time, resulting in sulfate reduction occurring exclusively within the first 70 cm by day 41, with 90% of that reduction occurring in the first 50 cm. No increase in aqueous sulfate concentrations is observed with distance along the column. This observation suggests that reoxidation of reduced sulfur species did not occur to any significant degree within the system.

The primary TEAP product species, Fe^{2+} and HS^- , were detected in effluent samples (Fig. 5), beginning on days 5 and 19, respectively. The concentration profiles demonstrate an initial period of iron reduction giving way to a subsequent period of sulfate reduction. The slow transition from high Fe^{2+} concentrations to high HS^- between days 20–34 agrees with the current conceptual model of the Old Rifle experiments in which multiple TEAPs are thought to operate in parallel during acetate augmentation (Yabusaki et al., 2011; Williams et al., 2011; Druhan et al., 2012). Sulfide concentrations are on the order of $40 \mu\text{M}$ on day 36, whereas sulfate concentrations on the same date decreased by roughly 8 mM over the length of the column. This imbalance requires a substantial amount of available iron to promote secondary sulfide mineral precipitation

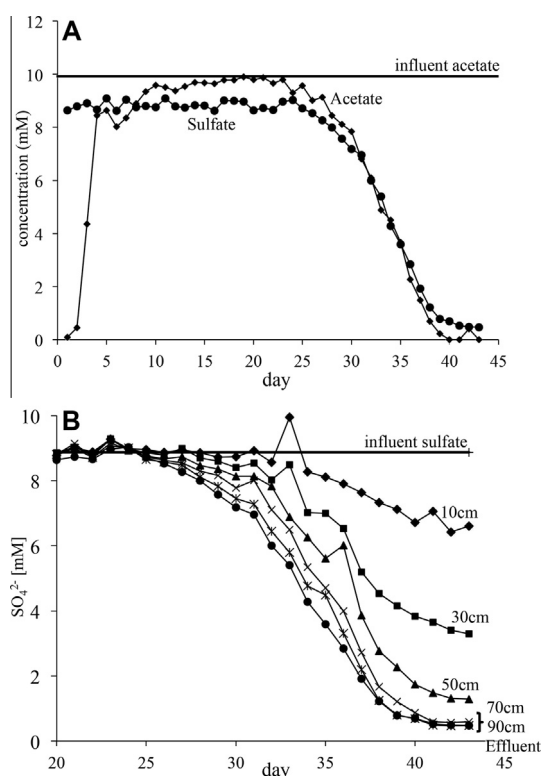


Fig. 4. (A) effluent sulfate (black circles) and acetate (black diamonds) concentration for the full 43 days of amendments, horizontal line indicates influent acetate concentration continuously supplied to the column. (B) SO_4^{2-} concentrations in all side ports and effluent for the final 23 days of acetate amendment, horizontal line indicates continuous influent sulfate concentration. All average measurement uncertainties are shown by the size of the data points.

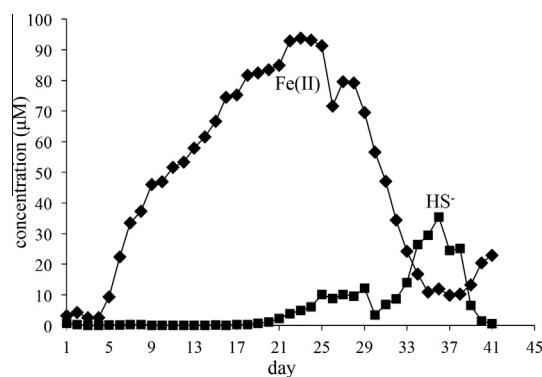


Fig. 5. Aqueous effluent Fe(II) and HS^- concentrations for the full 43 days of amendment. Data point size reflects average measurement uncertainty.

(Eqs. 1.2 and 1.3). The presence of secondary FeS precipitates was visually evident in the first 30 cm of the column, which turned a characteristic dark color as acetate amendment continued. This evidence suggests secondary mineral formation contributed to the observed 6% porosity reduction over the course of the experiment (Table 2). Between days 36–43, sulfide concentration declined and Fe^{2+} concentrations rebounded despite a constant removal rate of sulfate. This reversal corresponds with the approximate time at which sulfate reduction went essentially to completion over the first 70 cm; with the result that sulfide was no longer locally produced in the last 30 cm of the column. Therefore, this observation is considered a reflection of the abiotic sulfide oxidation – iron reduction pathway (Eq. 1.3) leading to consumption of aqueous sulfide, and generation of elemental sulfur and excess Fe^{2+} . If this pathway is actively influencing the measured effluent values of sulfide, the data demonstrate an example of a secondary influence on the measured sulfide concentrations between the point of sulfate reduction and the down-gradient measurement. At the field scale, decreased sulfide concentrations have been observed in down-gradient monitoring wells prior to cessation of acetate amendment (Druhan et al., 2008). The ability to observe the development of the sulfate reduction gradient and corresponding sulfide reactivity in the column experiment now indicates a likely pathway for sulfide removal leading to this observation.

4.3. Sulfur species $\delta^{34}\text{S}$

On the final day of acetate addition, sulfate $\delta^{34}\text{S}$ was enriched by 36‰ across the length of the column (Fig. 6A). At this time in the experiment, 10.5% of the total enrichment occurred within the first 10 cm, 19% occurred between 10–30 cm, and 28% occurred between 30–50 cm, resulting in a total of 57.5% of enrichment within the first half of the column. In comparison, on day 43, 90% of the total sulfate reduction occurred in the first 50 cm. The values of $\delta^{34}\text{S}$ in the final 30 cm of the column all fall within a close range of one another for the majority of the experiment. However, between days 39–43, the $\delta^{34}\text{S}$ of the effluent sulfate decreased slightly relative to the 70 and 90 cm side port samples. This observation is likely a result of minor amounts of sulfide re-oxidation in the effluent tubing, which had to be replaced as a result of clogging. As a consequence, effluent dissolved oxygen concentrations rose from 0.4 to 1.9 mg/L before rapidly returning to low values, likely in association with sulfide re-oxidation. Despite this 6‰ decrease in sulfate $\delta^{34}\text{S}$ between the 90 cm side port and the effluent at 100 cm on day 43, sulfide re-oxidation did not appear to have influenced sulfate concentrations in the effluent (Fig. 4B). This observation suggests the extent of sulfide re-oxidation was minor.

Effluent sulfide $\delta^{34}\text{S}$ values closely tracked the enrichment observed in effluent sulfate over the period of days 23–39 (Fig. 6B). Sulfide $\delta^{34}\text{S}$ was not collected outside this range of time due to a lack of sufficient concentration for stable isotope analysis (Fig. 5). Observed fractionation between sulfate and sulfide $\delta^{34}\text{S}$ varied from $\epsilon_{\text{meas}} = 11\text{--}14\text{‰}$ (Eq. 3.3) between days 23–37. None of the sulfate or sulfide

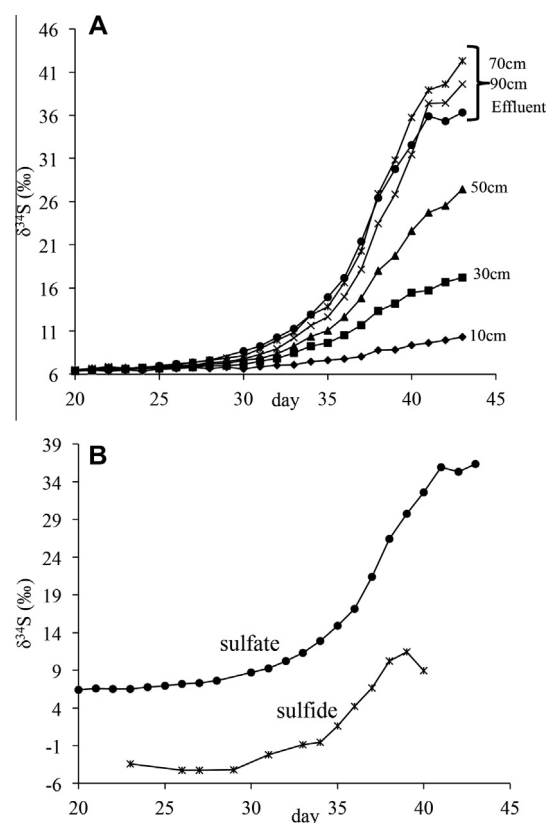


Fig. 6. (A) $\delta^{34}\text{S}$ of SO_4^{2-} in all side ports and effluent for the final 23 days of acetate amendment (B) $\delta^{34}\text{S}$ of SO_4^{2-} (reactant) and HS^- (product) in effluent. All measurement uncertainties are smaller than the size of the data points.

$\delta^{34}\text{S}$ time series collected along the length of the column fit a single Rayleigh fractionation model. This seemingly variable fractionation factor highlights the shortcomings of the Rayleigh distillation model in applications where rate laws are complex and supports incorporation of stable isotope fractionations into a model that can account mechanistically for these variations.

5. MODEL RESULTS AND DISCUSSION

5.1. Model parameters

The CrunchFlow code was used to develop a mechanistic simulation of the large column experiment. Iron reduction and sulfate reduction TEAPs were simulated (Table 3) using the dual-Monod rate law developed in Sections 2.1 and 2.3. The rate law for solid phase TEAPs used for iron reduction differs only in that the density term is replaced by a reactive surface area such that the maximum specific growth rate is entered in units of $\log(\text{moles}/\text{m}^2 \text{ cell/s})$. This version of the dual-Monod rate law is utilized in current field-scale models for Old Rifle uranium bioremediation (Fang et al., 2009; Yabusaki et al., 2011; Druhan et al., 2012). Incorporation of the stable isotopes of sulfur in the CrunchFlow code requires that the reactions affecting each isotopologue are solved explicitly in the model. As a

Table 3
Iron and sulfate reduction TEAP stoichiometry and associated parameters. Iron reduction is calculated using a bioavailable pool of ferrihydrite. Maximum specific utilization rates are in units of $\log(\text{mol}/\text{m}^2 \text{ cell}/\text{day})$ for iron reduction and $\text{mol}/\text{mol-C}_5\text{H}_7\text{O}_2\text{N}/\text{day}$ for sulfate reduction. Half saturation constants are consistent with the range of values from Dale et al. (2008) and Fang et al. (2009).

Stoichiometry	k_{max}	$K_{\text{s-half}}$ (mol/kgw)	$K_{\text{teap-half}}$ (mol/kgw)
$\text{Fe(III)}_{(\text{s})} + 0.208\text{CH}_3\text{COO}^- + 1.925\text{H}^+ + 0.033\text{NH}_4^+ \rightarrow 0.033\text{C}_5\text{H}_7\text{O}_2\text{N}_{\text{FERB}} + 1.600\text{H}_2\text{O} + 0.250\text{HCO}_3^- + \text{Fe}^{2+}$	2.7×10^{-5}	1.0×10^{-5}	
$\text{SO}_4^{2-} + 1.082\text{CH}_3\text{COO}^- + 3.050\text{H}^+ + 0.035\text{NH}_4^+ \rightarrow 0.033\text{C}_5\text{H}_7\text{O}_2\text{N}_{\text{SRB}} + 2.100\text{H}_2\text{O} + 2\text{CO}_{2(\text{aq})} + \text{H}_2\text{S}_{(\text{aq})}$	3.31×10^2	1.0×10^{-4}	5.0×10^{-3}

result the dual-Monod rate law for sulfate reduction is solved independently for the $^{32}\text{SO}_4$ and $^{34}\text{SO}_4$ “species” (Eq. 2.18a and b), although the two reactions are coupled through a single enzymatic pathway, as discussed above (Section 2.3). The maximum specific utilization rate for the $^{34}\text{SO}_4$ reduction reaction (Eq. 2.18b) was set to $3.268 \times 10^2 \text{ mol}/\text{mol-C}_5\text{H}_7\text{O}_2\text{N}/\text{day}$ such that, in comparison with the common $^{32}\text{SO}_4$ rate constant (Table 3), the simulated kinetic fractionation factor (the ratio of the rate constants, as in Eq. 2.18) was $\alpha_k = 0.987$. It is important to note that this value was not fit to the current dataset. Instead, it was taken directly from a field scale study of sulfate $\delta^{34}\text{S}$ enrichment at the Old Rifle field site (Druhan et al., 2012). In keeping with previous models of sulfur isotope systematics at Old Rifle, fractionation associated with mackinawite (Eq. 1.2) and elemental sulfur (Eq. 1.3) formation is considered negligible. Thus kinetic fractionation associated with DSR is the only fractionating process considered in the model.

Iron reduction was modeled as a single Monod rate based on field evidence that Fe(III)-bearing (oxy)hydroxides remain abundant following multiple electron donor amendments (Li et al., 2009). In keeping with methods currently utilized for biogeochemical models of field scale acetate amendment at Old Rifle, both iron and sulfate reduction were allowed to proceed from the start of the simulation (i.e. no inhibition for either species), though a much lower starting SRB was used to produce a lag in the onset of sulfate reduction, and a zero-order biomass decay term was employed for the SRB population (Yabusaki et al., 2011; Druhan et al., 2012), at a rate of $2.2 \times 10^{-3} \text{ day}^{-1}$. A yield factor of 40% was employed for iron reduction and 8% for sulfate reduction stoichiometry (Rittmann and McCarty, 2001; Li et al., 2009), such that for sulfate reduction 92% of acetate oxidation was partitioned to the catabolic pathway and 8% was partitioned to anabolic growth.

Abiotic heterogeneous reactions, associated rate constants and solubility products are shown in Table 4. Initial conditions were established based on the steady state solute concentrations of the influent and effluent solutions prior to the start of acetate addition (Table 5). Influent boundary conditions differed from initial conditions only in that acetate increased to 9.75 mmol/kgw, bromide increased to 1.32 mmol/kgw, sodium increased to 22.0 mmol/kgw and potassium increased to 1.58 mmol/kgw. In addition the influent solution contained no biomass. The initial mineral assemblage was based on typical compositions utilized for field-scale models (Table 6; Li et al., 2009, 2010). Non-reactive quartz was used to fill the remaining volume fraction to achieve a porosity of 0.33. Speciation reactions and associated equilibrium constants included in the model are provided in Appendix E.

The model domain is 1D, consisting of 100 grid blocks of 1.0 cm length. Flow is calculated by assigning a permeability of $1.08 \times 10^{-12} \text{ m}^2$ over a pressure gradient of $1.614 \times 10^3 \text{ Pa}$ to produce a Darcy flow rate of 0.15 m/day. The code updates the permeability of the system based on a cubic law relationship with porosity, which decreases as a function of mineral and biomass growth over the course of the simulation. While the vast majority of model

Table 4

Heterogeneous reactions and associated parameters for the mesoscale column simulation.

Stoichiometry	log k (mol/m ² /s)	log K _{sp}
$\text{CaCO}_{3(s)} \leftrightarrow \text{Ca}^{2+} + \text{CO}_3^{2-}$	−4.1	−8.4801
$\text{MgCO}_{3(s)} + \text{H}^+ \leftrightarrow \text{Mg}^{2+} + \text{HCO}_3^-$	−8.4	2.9734
$\text{Fe}^{2+} + \text{H}_2\text{S}_{(\text{aq})} \leftrightarrow \text{FeS}_{(\text{am})} + 2\text{H}^+$	−8.0	3.5
$\text{Fe}(\text{OH})_{3(s)} + \text{H}_2\text{S}_{(\text{aq})} + 2.5\text{H}^+ \leftrightarrow \text{Fe}^{2+} + 0.5\text{S}_{(\text{s})} + \text{H}_2\text{O} + 2\text{OH}^-$	−7.5	−19.6
$\text{C}_5\text{H}_7\text{O}_2\text{N}_{\text{FeRB}} \leftrightarrow \text{C}_5\text{H}_7\text{O}_2\text{N}_{\text{FeRB}(\text{aq})}$	−2.0	−15.0
$\text{C}_5\text{H}_7\text{O}_2\text{N}_{\text{SRB}} \leftrightarrow \text{C}_5\text{H}_7\text{O}_2\text{N}_{\text{SRB}(\text{aq})}$	−2.0	−15.0

Table 5

Initial conditions of aqueous primary species for the start of the mesoscale column simulation.

Primary species	Concentration (mmol/kg H ₂ O)
pH	7.2
Fe^{2+}	1.0E−08
Fe^{3+}	In equilibrium with iron hydroxide
$\text{SiO}_{2(\text{aq})}$	0.35
Na^+	10.6
K^+	0.447
Ca^{2+}	5.30
Mg^{2+}	5.41
SO_4^{2-}	8.8
Cl^-	3.0
$\text{CO}_{2(\text{aq})}$	9.0
Acetate	0.0
$\text{H}_2\text{S}_{(\text{aq})}$	1.0E−15
$\text{O}_{2(\text{aq})}$	15.6E−03
NH_4^+	1.0
Br^-	0.0
Methane _(aq)	1.0E−15

Table 6

Initial conditions of mineral volume fraction for the start of the mesoscale column simulation.

Mineral	Volume fraction (m ³ /m ³)
Ferrihydrite	3.0E−03
Goethite	3.6E−04
Calcite	4.7E−04
Magnesite	1.0E−06
$\text{Fe}(\text{OH})_3$	1.9E−03
$\text{C}_5\text{H}_7\text{O}_2\text{N}_{\text{FeRB}}$	9.0E−05
$\text{C}_5\text{H}_7\text{O}_2\text{N}_{\text{SRB}}$	1.0E−07
Quartz	0.62

parameters are taken from previous field-scale reactive transport models of biostimulation at the Old Rifle field site (Li et al., 2009; Fang et al., 2009; Yabusaki et al., 2011; Druhan et al., 2012), the specific rate of sulfate reduction appropriate for these trenched, sieved and repacked sediments was fit to the effluent sulfate and acetate concentrations measured in the column experiment.

5.2. Effluent concentrations and $\delta^{34}\text{S}$

Simulated effluent acetate and sulfate concentration profiles reproduce the observed trends in the column experiment, including the accelerated consumption of acetate relative to sulfate at late time (Fig. 7A). Neither the activity

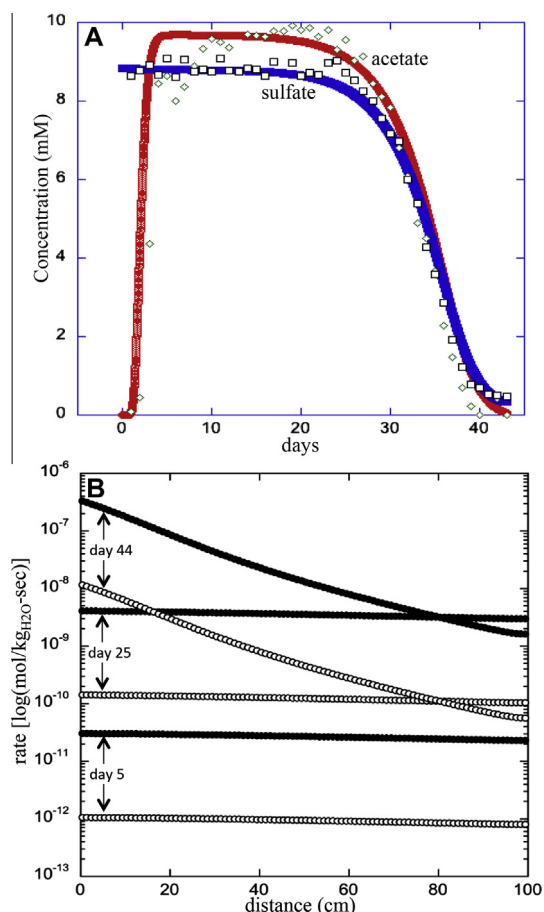


Fig. 7. (A) simulated effluent acetate (red) and sulfate (blue) for the full 43 days of organic carbon amendment plotted in comparison with measured effluent acetate (white diamonds) and sulfate (white squares). Both modeled and measured values indicate acetate became the limiting nutrient at late time during sulfate reduction. (B) Simulated rates of sulfate reduction (black line) and SRB growth (white circles) across the length of the column on days 5, 25 and 44 of acetate amendment. (For interpretation of the references to colour in this figure legend, the reader is referred to the web version of this article.)

of iron reducers or the decay term imposed on the SRB population strongly influences the simulated acetate profiles for the rates of reaction used here. Carbon isotope mass balance calculations suggest that a secondary organic carbon process may be active during the iron reduction phase, but this effect is not anticipated to influence DSR and has

not been included in the current simulations (Druhan et al., 2014 companion paper). The excess consumption of acetate relative to sulfate in the simulations is thus entirely due to the anabolic component of DSR. This anabolism serves to heighten the acetate oxidation rate as well as the overall sulfate reduction rate over time as a result of increased SRB. This relationship is demonstrated by comparison of the rates of aqueous sulfate reduction (catabolic pathway) and SRB growth (anabolic pathway) over time across the domain (Fig. 7B). The offset between the rate of sulfate reduction and the rate of SRB growth is constant throughout the simulation, reflecting the specified yield factor. The effluent dataset and corresponding model provide the first direct evidence to support the use of an 8% yield factor (Rittmann and McCarty, 2001) for SRB growth under Old Rifle conditions. Furthermore, the rates of sulfate reduction and SRB growth (Fig. 7B) evolve from constant values across the length of the domain at early time, to decreasing values from inlet to outlet at late time. This trend reflects the total consumption of acetate across the length of the column, thus limiting further growth of the SRB population and correspondingly the rate of sulfate reduction in the effluent end of the column after roughly day 40. This gradient in sulfate reduction and SRB growth rates was also suggested at the field scale (Druhan et al., 2012) and is further confirmed by these model results.

Simulated effluent product species of the iron and sulfate reduction reactions show good agreement with measured values of aqueous Fe^{2+} and sulfide (Fig. 8). The production of Fe^{2+} occurs with a minimal decline in the simulated acetate concentration because of the 8:1 molar ratio of Fe(III) to acetate consumption. In addition, when sulfide begins to

be produced in the model as early as day 12, Fe^{2+} is also generated via the elemental sulfur reaction pathway (Eq. 1.3). As a result, modeled iron hydroxide reduction may proceed through both biotic and abiotic pathways, leading to less overall $\text{C}_5\text{H}_7\text{O}_2\text{N}_{\text{FeRB}}$ biomass growth despite a large production of aqueous Fe^{2+} . Simulated sulfide concentrations increase above Fe^{2+} concentrations on day 35, in good agreement with measured values. The model also reproduces the observed decrease in sulfide concentrations at late time as a result of the FeS and elemental sulfide pathways (Eqs. 1.2 and 1.3) in the last 30 cm of the column.

Simulated $\delta^{34}\text{S}$ evolution of the effluent sulfate and sulfide reproduce observed trends in the measured data (Fig. 9). The sulfate $\delta^{34}\text{S}$ reflects a cumulative isotopic ratio of reactant remaining in solution, whereas the highly reactive sulfide behaves close to an instantaneous isotopic ratio of the product species. Several important conclusions are drawn from these results. First, the modified dual-Monod rate expressions developed in Section 2.3 are able to reproduce the observed enrichment in reactant and product $\delta^{34}\text{S}$ across a wide range of sulfate concentrations using a single kinetic fractionation factor. The model also accounts for additional influences on the resultant observed enrichment of $\delta^{34}\text{S}$, for example during high sulfide production the ratio of sulfide $^{34}\text{S}/^{32}\text{S}$ may become somewhat cumulative rather than a truly instantaneous value. As a result the simulated ratio of fluid $(^{34}\text{HS}^-/^{32}\text{HS}^-)/(^{34}\text{SO}_4^{2-}/^{32}\text{SO}_4^{2-})$ is variable while the underlying fractionation factor α_p is constant. Second, simulated $\delta^{34}\text{S}$ of both sulfate and sulfide after day 39 over predicts corresponding measured values. This discrepancy may be attributed to either (1) a minor amount of sulfide re-oxidation, (2) a sulfur disproportionation-

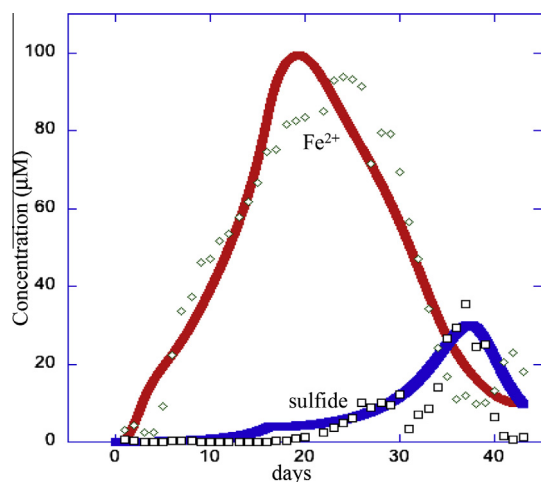


Fig. 8. Simulated effluent Fe^{2+} (red) and sulfide (blue) for the full 43 days of organic carbon amendment plotted in comparison with measured effluent Fe^{2+} (white diamonds) and sulfide (white squares). At early time iron reduction is the predominant TEAP, but sulfate reduction rates increase and become dominant at late time. The decline in sulfide concentration after day 37 is associated with complete consumption of acetate across the length of the column, thus leading to decreased sulfide production near the outlet. (For interpretation of the references to colour in this figure legend, the reader is referred to the web version of this article.)

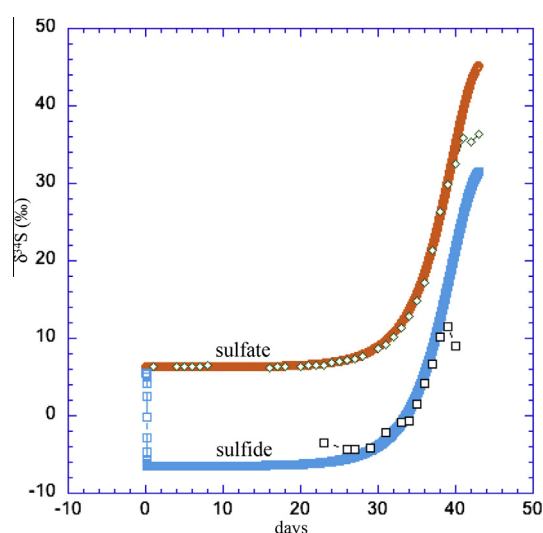


Fig. 9. Simulated effluent $\delta^{34}\text{S}$ values of sulfate (orange) and sulfide (light blue) for the full 43 days of organic amendment plotted in comparison with measured effluent $\delta^{34}\text{S}$ of sulfate (white diamonds) and sulfide (white squares). The kinetic fractionation factor used to produce this model is equal to the value measured in a field scale experiment at the Old Rifle site (Druhan et al., 2012). (For interpretation of the references to colour in this figure legend, the reader is referred to the web version of this article.)

ation pathway or (3) to a true change in the kinetic fractionation factor as a result of substrate limitation. Sulfur disproportionation has been demonstrated for acetate supplemented DSR (Detmers et al., 2001) and this pathway cannot be ruled out with the current dataset, however, the accurate match between modeled 8% yield factor and measured effluent sulfate and acetate concentrations suggests that this pathway is unnecessary to describe the system. These influences will be further explored in Section 5.3. Third, sensitivity analysis of modeled $\delta^{34}\text{S}$ demonstrates that in order to simultaneously reproduce the isotopic trends of both sulfate and sulfide, the rate constants and fractionation factor must be precisely known. For example, if the rate constant for $^{32}\text{SO}_4$ reduction (k_{max} , Table 3) is increased by 2%, without altering the corresponding rate constant for $^{34}\text{SO}_4$, then the kinetic fractionation factor shifts from 0.987 to 0.968, an increase of 19‰. This leads to a much larger simulated enrichment of both sulfate and sulfide $\delta^{34}\text{S}$ than is observed in the measured data. If the rate constant for $^{34}\text{SO}_4$ is then increased to reproduce the correct kinetic fractionation factor (0.987), the model may accurately simulate the enrichment in $\delta^{34}\text{S}$ of sulfate, but the offset of the modeled $\delta^{34}\text{S}$ sulfide from $\delta^{34}\text{S}$ sulfate will also be smaller, by up to 3‰, and the measured values of sulfide $\delta^{34}\text{S}$ will not be reproduced. As a result, in order to simulate both the reactant and product enrichments, the maximum specific yields of the $^{32}\text{SO}_4$ and $^{34}\text{SO}_4$ must be correct both in magnitude and ratio. Given this relationship and the accurate reproduction of measured $\delta^{34}\text{S}$ using a kinetic fractionation factor from previous field-scale studies, we find that the explicit inclusion of stable isotopes of sulfur increases sensitivity to the overall reduction rate and thus provides improved precision for the biostimulation reactive transport model. Thus we conclude the maximum specific yield factors used in the model (Table 3) are accurate for sulfate reduction at the Old Rifle site as reproduced in the laboratory column experiment.

5.3. Spatial profiles of SO_4 and $\delta^{34}\text{S}$

Often the analysis of near-surface geochemical processes is based upon fluid samples collected over time at discrete locations. The Old Rifle bioremediation field experiments are an example of this situation (Section 1.1) in which monitoring wells are located several meters down-gradient of the point source of organic carbon amendment. The fluid chemistry and corresponding model results of the column effluent are in some sense like a monitoring well located 100 cm down gradient of the acetate source. Here we present the first comparison of simulated geochemical and stable isotope variations to direct measurements in the highly reactive zone immediately adjacent to the organic carbon source. No adjustment to the model parameters were made from those presented in Sections 5.1 and 5.2 so that we can observe the extent to which the 1D homogeneous model is capable of reproducing spatial development of the observed sulfate reduction gradient in the experimental system.

Simulated sulfate concentration and $\delta^{34}\text{S}$ profiles at distances of 10 cm (Fig. 10A), 30 cm (Fig. 10B), 50 cm (Fig. 10C), 70 cm (Fig. 10D) and 90 cm (Fig. 10E) in the

model domain are compared with the concentration profiles and measured $\delta^{34}\text{S}$ values from the corresponding side ports. Agreement between modeled and measured values is extremely good in all locations for roughly the first 30 days of acetate augmentation. Following this period (particularly beyond day 40) the model over predicts sulfate removal and corresponding $\delta^{34}\text{S}$ enrichment in the first 50 cm of the column, but accurately reproduces measured values at 70 cm and 90 cm. This observation seems to suggest that the modeled half saturation constant is causing a delayed transition to the higher order rate expression. However, variation of the half-saturation constants within the range of parameters specified by Dale et al. (2008) and Fang et al. (2009) could not produce an improvement in the 10 and 30 cm simulated solute profiles. As a result the dampened reduction rate measured in the 10 and 30 cm side ports relative to the simulated profiles are thought to result from heterogeneity unaccounted for in the 1D model. This heterogeneity may be physical or microbial in nature. Dividing the model domain into sections and assigning unique starting compositions to each, it is possible to improve the fit of the simulated concentration profile by either reducing the initial SRB or increasing permeability in the first 20 cm. The population and distribution of the sulfate reducing biomass is explored further in the companion paper (Druhan et al., 2014 companion paper).

The sulfate $\delta^{34}\text{S}$ data obtained from the side ports is also helpful in demonstrating the pitfalls associated with application of a simple Rayleigh model to the current dataset. Using the effluent time series, a fairly reasonable fit can be achieved with a Rayleigh model fractionation of approximately 10‰. However, applying the same treatment to the time series of the side ports demonstrates that near the inlet the data correspond to a higher fractionation of approximately 12‰ and appear to transition to lower values along the length of the column. As we demonstrate using the isotope-specific dual-Monod derivation, the entire spatiotemporal dataset can be accurately reproduced with a single kinetic fractionation of 13‰, thus emphasizing the fact that a Rayleigh model yields a fractionation that is essentially an observational average and an underestimate of the true α (Van Breukelen and Prommer, 2008).

Comparing the measured and simulated spatial profiles of sulfate $\delta^{34}\text{S}$ results in a second important observation. In the 70 and 90 cm side ports, simulated $\delta^{34}\text{S}$ accurately reproduces the trend and magnitude of measured enrichment throughout the complete 43-day experiment. This result demonstrates that the modified dual-Monod expressions developed for this model (Section 2.3) are capable of simulating $\delta^{34}\text{S}$ enrichment using a single kinetic fractionation factor down to a sulfate concentration of <0.47 mM. This brings the total sulfate concentration close to the half saturation constant for the model (Table 3) and thus involves a transition in reaction order. It is important to note that using our improved Monod formulation (Eq. 2.18a and b), we have successfully simulated this transition from zero-order to first-order regimes, because the two isotopologues are properly linked to each other. Earlier studies have used two fully independent Monod equations of the form in Eq. 2.8 without this rigorous coupling (e.g. Dale

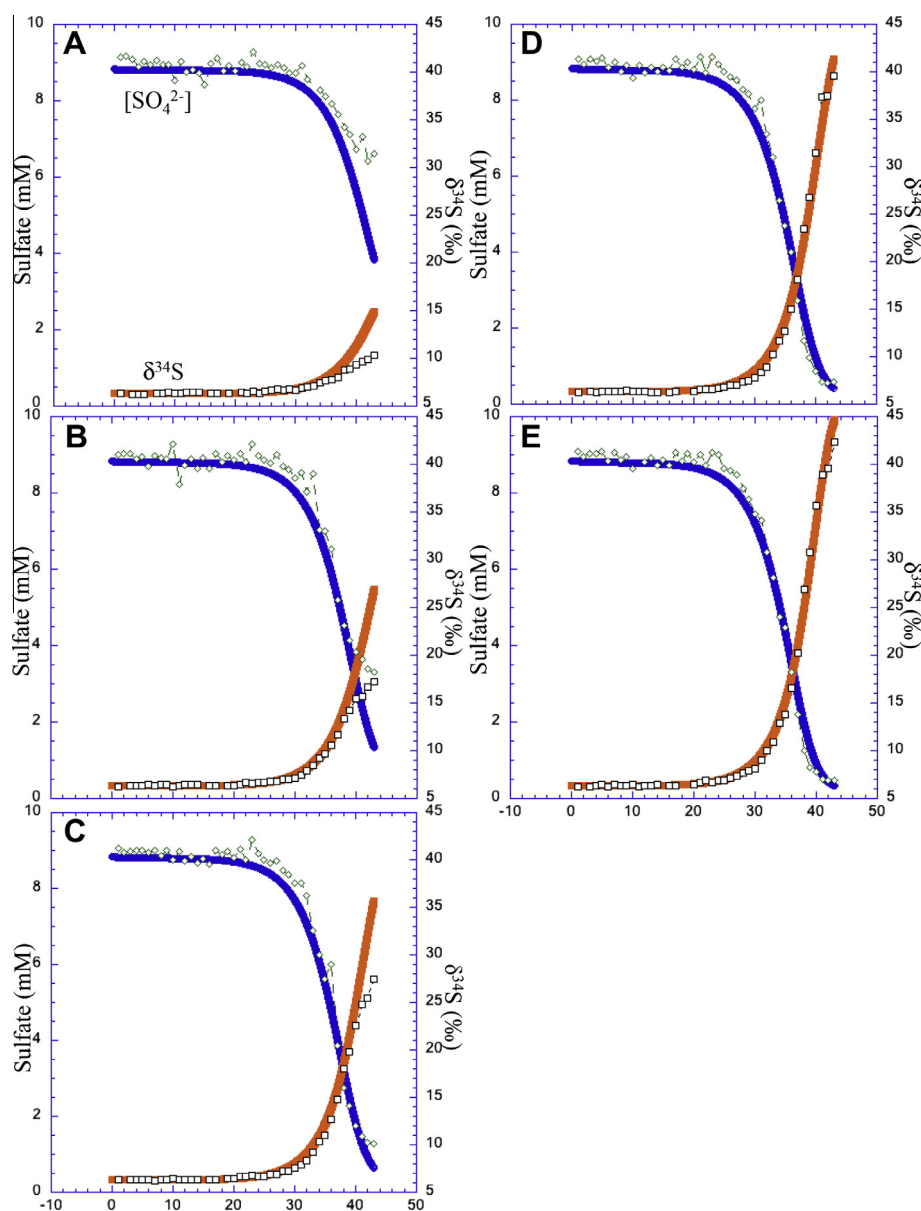


Fig. 10. Simulated sulfate concentrations (blue) and $\delta^{34}\text{S}$ values (orange) plotted in comparison with measured values for all distances along the length of the column: (A) 10 cm, (B) 30 cm, (C) 50 cm, (D) 70 cm and (E) 90 cm. (For interpretation of the references to colour in this figure legend, the reader is referred to the web version of this article.)

et al., 2009; Gibson et al., 2011; Wehrmann et al., 2013), which may have limited these models to either zero-order or first-order conditions, and in some cases prevented accurate simulation of the transition in reaction order.

Finally, accurate simulation of the magnitude of sulfate $\delta^{34}\text{S}$ enrichment in the 70 and 90 cm side ports indicates that the modeled $\delta^{34}\text{S}$ which exceeded measured values in the effluent (Fig. 9) is likely due to a minor amount of sulfide reoxidation in the effluent tubing instead of a variation in the kinetic fractionation factor or a sulfur disproportionation pathway. Based on a comparison of measured and simulated $\delta^{34}\text{S}$ values, this reoxidation would contribute roughly 0.1 mM to the effluent sulfate concentration, an increase too minor to observe in the concentration measurements (Fig. 4B).

5.4. Elemental sulfur $\delta^{34}\text{S}$

As discussed in the introduction (Section 1.1) the accumulation of reduced sulfur species has been suggested as a mechanism for long-term U stabilization. Both mackinawite and elemental sulfur generated during DSR activity are isotopically distinct from the background $\delta^{34}\text{S}$ composition of sulfate in the aquifer. Thus reoxidation of these species associated with long-term U stabilization may be potentially predicted and monitored through their characteristic isotopic signature. Such a method would provide evidence for re-oxidation of solids specifically generated during the electron donor amendment, and would have important application to the study of long-term contaminant stabilization. Simulated elemental sulfur accumulation

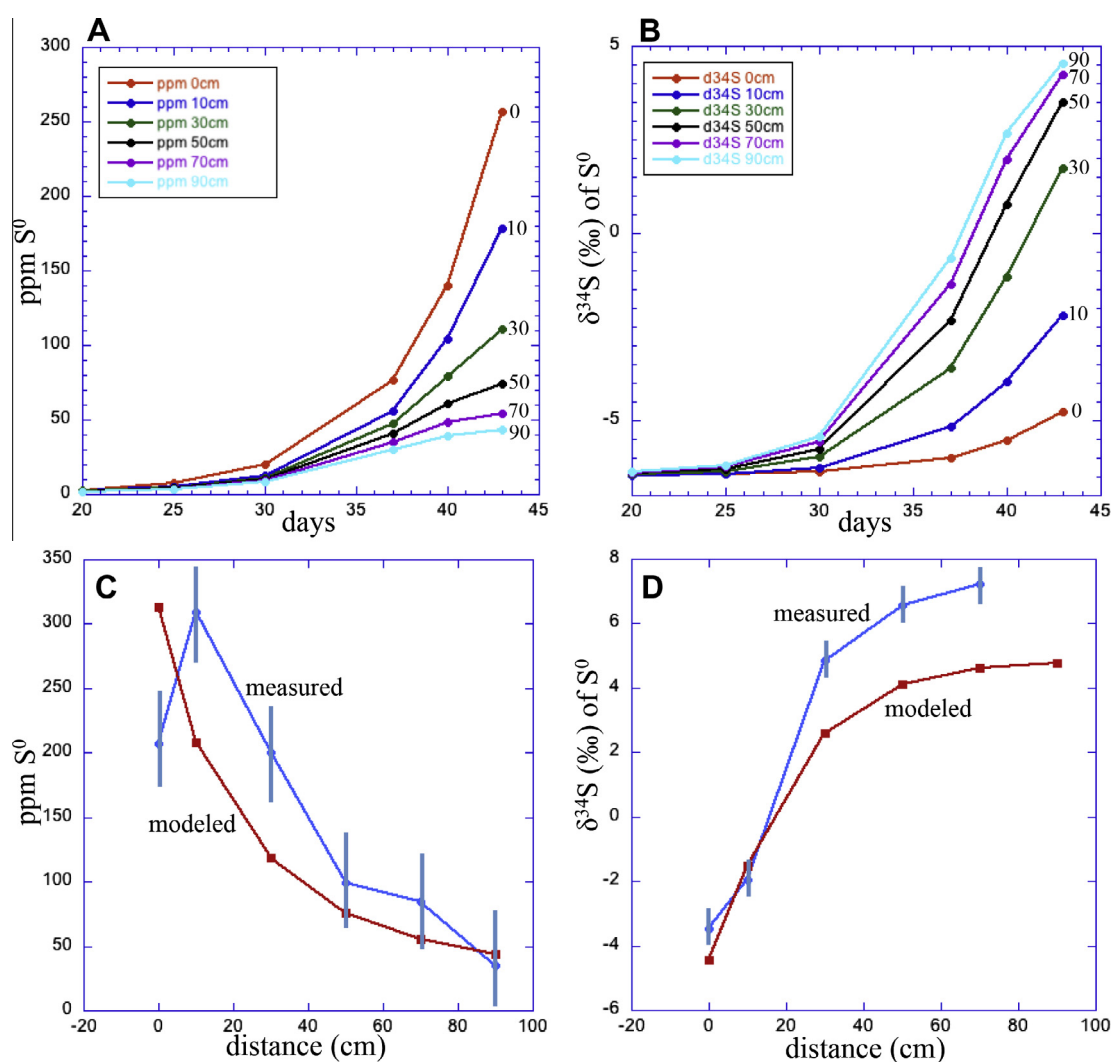


Fig. 11. Simulated solid phase elemental sulfur (A) by weight and (B) $\delta^{34}S$ for the final 23 days of organic carbon amendment. Lines are labeled to indicate distances (cm) along the length of the column. Solid phase samples were recovered after 43 consecutive days of organic carbon amendment and measured values of elemental sulfur (C) by weight and (D) $\delta^{34}S$ are plotted with corresponding model values with measurement uncertainty shown.

with distance along the column (Fig. 11A) predicts the majority of material will accumulate near the organic carbon source. At 0 cm the simulation showed an increased S^0 of 261 ppm by weight over the 43-day period. In contrast an increase of only 44 ppm was predicted at 90 cm. This distribution again reflects the reactivity of aqueous sulfide in the system via the reaction pathways described in Eqs. 1.2 and 1.3. In particular, after day 30 of acetate addition, DSR occurred almost exclusively in the first half of the column, leading to substantial accumulation of secondary sulfide minerals in the area adjacent to the influent. Simulated $\delta^{34}S$ of this elemental sulfur pool reflects the distillation of sulfate $\delta^{34}S$ with distance down the column (Fig. 11B). Values near the inlet are low, increasing from a background of -6.4‰ to -4.4‰ at the inlet, and 4.8‰ at 90 cm. Again the majority of this enrichment takes place within the first 50 cm of the column.

Sediments recovered from the column after the 43-day experiment provide a direct comparison to simulated val-

ues. Measured solid phase elemental sulfur (Fig. 11C) at all locations were substantially higher than a background sample of Old Rifle sediment (0.3 ppm) that was not packed into the column. Measured values also decreased from the inlet to the effluent end of the column, and showed fairly good agreement with the simulated trend. The model generally underestimated the measured values, despite the fact that the spatial profiles of sulfate concentration and sulfate $\delta^{34}S$ (Section 5.3) indicated that the model overpredicted DSR in the first 50 cm of the column after roughly day 30. These results indicate that the rate of elemental sulfur formation in the system is likely higher than the current model parameters, suggesting that even more aqueous Fe^{2+} is generated via the abiotic iron reduction pathway (Eq. 1.3) relative to microbial iron reduction. Measured $\delta^{34}S$ of elemental sulfur (Fig. 11D) also showed a trend in good agreement with simulated values. The model correctly reproduced values near the inlet of the column, where the vast majority of elemental sulfur accumulated. At further

distances the model underestimated the $\delta^{34}\text{S}$ values, though these samples had relatively low elemental sulfur content and were thus more susceptible to contamination by enriched sulfate. The ability of the model to reproduce measured $\delta^{34}\text{S}$ values of elemental sulfur in the region of highest accumulation demonstrates that these simulations can be utilized to predict the isotopic shifts in sulfate associated with re-oxidation.

6. SUMMARY

The model demonstrated here features a modification to the dual-Monod rate expression such that the sulfur isotopologues of sulfate can be individually resolved to simulate sulfur isotope fractionation. Using this framework, our study indicates that models failing to account for the coupled behavior of isotopologues in Monod kinetics can lead to spurious results (which may appear to indicate a variable fractionation factor) when in fact the model is inaccurately simulating the transition across reaction order. Therefore an important contribution of this study is a more generalized form of isotope-specific Monod-type rate expression that operates at both high and low substrate concentrations (relative to the half saturation constant). In addition this model allows for growth and decay of the sulfate reducing biomass population as demonstrated in field-scale applications (Druhan et al., 2012). As a result, this study has shown accurate simulation of DSR and associated $\delta^{34}\text{S}$ enrichment from high sulfate concentrations down to a final value of <0.5 mM. Furthermore the model is capable of reproducing both spatial and temporal profiles in sulfate and sulfide $\delta^{34}\text{S}$ over the full range of experimental conditions using a single fractionation factor taken from field measurements at the Old Rifle site. This result indicates that the experimental design reproduced field parameters contributing to $\delta^{34}\text{S}$ enrichment. This improved ability to model fractionation of the reactant and product species simultaneously within a multi-component reactive transport code presents novel opportunities for analysis of field scale isotopic datasets.

The design of the column experiment afforded high-resolution sampling that captured spatial and temporal development of the DSR gradient across the length of the column. These data provide a rare view into the highly reactive zone immediately adjacent to a nutrient source and suggests that the current model could be improved by incorporating physical and biological heterogeneity. Despite this discrepancy the simulation accurately captured aqueous sulfur species and $\delta^{34}\text{S}$ trends across the column and was extended to predict the associated accumulation and isotopic distribution of solid phase elemental sulfur. Simulated elemental sulfur showed good agreement in magnitude and trend with measured values of solid phase samples recovered from the column. In particular the model reproduced the $\delta^{34}\text{S}$ of elemental sulfur in the region of highest accumulation. This result implies the capacity to predict the $\delta^{34}\text{S}$ signal associated with re-oxidation of reduced sulfur minerals, and potentially yields a new means of monitoring stability of secondary minerals in subsurface environments. Furthermore, this potential isotopic signal of

reoxidized sulfur species has important implications for studying the long-term stability of heavy metal species in previously augmented systems. To our knowledge this is the first numerical model to demonstrate such rigorous treatment of stable isotope ratios in the cycling of a redox-sensitive element.

ACKNOWLEDGMENTS

Design, fabrication and execution of the large column experiment was greatly aided by the advice and assistance of Joern Larsen, Yuxin Wu, Li Yang, April Van Hise, Shaun Brown, Peter Nico and Jonathan Ajo-Franklin. The authors wish to thank the AE Jack Middelburg, Pierre Regnier, Benjamin Brunner and one anonymous reviewer for their constructive comments. This research was supported as part of the Sustainable Systems Scientific Focus Area at the Lawrence Berkeley National Laboratory funded by the U.S. Department of Energy, Office of Science, Office of Biological and Environmental Research, Subsurface Biogeochemical Research program under award number DE-AC02-05CH11231 and by the U.S. Department of Energy, Office of Science, Subsurface Biogeochemical Research program through the Integrated Field Research Challenge (IFRC) at Rifle, Colorado.

APPENDIX A

Deuterium and ^{18}O tracer breakthrough data.

Starting day	Hour	Location	$\delta^2\text{H}$ (‰)	$\delta^{18}\text{O}$ (‰)
1	0	10 cm	−68.22	−14.17
1	0	30 cm	−78.40	−11.63
1	0	50 cm	−84.21	−12.18
1	0	70 cm	−86.29	−12.21
1	0	90 cm	−85.20	−12.11
1	0	Effluent	−86.50	−12.22
1	6	10 cm	266.07	−11.37
1	6	30 cm	−74.19	−12.12
1	6	50 cm	−83.35	−12.14
1	6	70 cm	−86.25	−12.14
1	6	90 cm	−87.98	−12.12
1	6	Effluent		
1	12	10 cm	422.33	−12.14
1	12	30 cm	53.02	−12.18
1	12	50 cm	−78.00	−12.11
1	12	70 cm	−83.15	−12.06
1	12	90 cm	−77.24	−9.53
1	12	Effluent	−85.51	−12.14
1	24	10 cm	444.36	−12.03
1	24	30 cm	372.76	−12.16
1	24	50 cm	110.49	−12.09
1	24	70 cm	−23.99	−12.11
1	24	90 cm	−67.30	−9.85
1	24	Effluent	−80.90	−12.18
1	48	10 cm	453.73	−12.12
1	48	30 cm	468.98	−12.16
1	48	50 cm	431.81	−12.08
1	48	70 cm	347.17	−12.10
1	48	90 cm	210.69	−12.16
1	48	Effluent	135.40	−12.22
1	72	10 cm	451.71	−9.75

(continued on next page)

Appendix A (continued)

Starting day	Hour	Location	$\delta^2\text{H}$ (‰)	$\delta^{18}\text{O}$ (‰)
1	72	30 cm	471.85	−12.18
1	72	50 cm	472.75	−11.84
1	72	70 cm	459.97	−11.96
1	72	90 cm	411.17	−12.17
1	72	Effluent	357.76	−12.15
1	96	10 cm	471.23	−12.08
1	96	30 cm	472.85	−12.12
1	96	50 cm	476.71	−12.10
1	96	70 cm	477.62	−12.10
1	96	90 cm	470.69	−12.09
1	96	Effluent	463.61	−12.16
24	0	10 cm	478.99	−12.23
24	0	30 cm	479.78	−12.14
24	0	50 cm	480.26	−12.17
24	0	70 cm	478.62	−12.17
24	0	90 cm	475.18	−11.90
24	0	Effluent	474.48	−11.63
24	9.5	10 cm	481.31	10.18
24	9.5	30 cm	479.12	−3.97
24	9.5	50 cm	474.22	−11.20
24	9.5	70 cm	470.71	−12.15
24	9.5	90 cm	478.63	−12.18
24	9.5	Effluent	481.00	−12.24
24	25	10 cm	477.49	15.56
24	25	30 cm	476.75	9.23
24	25	50 cm	478.13	−0.08
24	25	70 cm	481.37	−7.47
24	25	90 cm	477.64	−11.07
24	25	Effluent	476.18	−11.90
24	49	10 cm	480.88	15.66
24	49	30 cm	481.26	15.15
24	49	50 cm	480.44	9.53
24	49	70 cm	476.69	5.23
24	49	90 cm	476.92	−1.34
24	49	Effluent	478.18	−5.18
24	73	10 cm	480.43	15.74
24	73	30 cm	479.87	15.79
24	73	50 cm	477.73	14.33
24	73	70 cm	472.52	12.82
24	73	90 cm	477.67	9.01
24	73	Effluent	481.25	4.89
24	99	10 cm	444.51	15.69
24	99	30 cm	468.07	15.68
24	99	50 cm	472.16	15.36
24	99	70 cm	444.89	15.16
24	99	90 cm	466.01	14.31
24	99	Effluent	475.13	12.16
24	124	10 cm	475.49	15.82
24	124	30 cm	477.58	15.84
24	124	50 cm	477.19	15.82
24	124	70 cm	477.31	15.69
24	124	90 cm	476.27	15.37
24	124	Effluent	476.06	14.63
40	0	10 cm	475.67	15.81
40	0	30 cm	474.20	15.70
40	0	50 cm	475.80	15.80
40	0	70 cm	475.92	15.78
40	0	90 cm	474.98	15.77
40	0	Effluent	478.15	15.76
40	6	10 cm	473.15	1.95
40	6	30 cm	476.66	12.95

(continued on next page)

Appendix A (continued)

Starting day	Hour	Location	$\delta^2\text{H}$ (‰)	$\delta^{18}\text{O}$ (‰)
40	6	50 cm	474.81	15.73
40	6	70 cm	476.86	15.75
40	6	90 cm	476.63	15.74
40	6	Effluent	474.33	15.68
40	12	10 cm	478.07	−9.00
40	12	30 cm	475.22	5.66
40	12	50 cm	477.63	14.14
40	12	70 cm	474.69	15.76
40	12	90 cm	475.70	15.76
40	12	Effluent	476.31	15.73
40	24	10 cm	473.52	−11.87
40	24	30 cm	478.44	−5.31
40	24	50 cm	474.19	4.36
40	24	70 cm	477.71	12.02
40	24	90 cm	476.41	15.05
40	24	Effluent	476.57	15.57
40	50	10 cm	477.53	−12.09
40	50	30 cm	474.26	−11.75
40	50	50 cm	478.13	−6.77
40	50	70 cm	475.14	−2.84
40	50	90 cm	477.70	3.90
40	50	Effluent	476.01	8.05
40	78	10 cm	475.84	−12.12
40	78	30 cm	477.83	−12.08
40	78	50 cm	474.04	−11.44
40	78	70 cm	478.52	−10.22
40	78	90 cm	475.11	−6.96
40	78	Effluent	478.22	−3.83

APPENDIX B

Anion concentration measurements for all side ports and effluent

Day	Location	Acetate (mM)	Cl (mM)	Br (mM)	SO ₄ (mM)
1	10 cm	6.66	2.90	1.15	9.13
2	10 cm	7.29	2.92	1.17	9.17
3	10 cm	7.12	2.85	1.31	9.08
4	10 cm	6.78	2.79	1.29	8.90
5	10 cm	7.80	2.96	1.27	9.03
6	10 cm	7.67	2.94	1.27	8.95
7	10 cm	7.78	2.94	1.27	9.07
8	10 cm	7.57	2.87	1.24	8.95
9	10 cm	6.24	2.66	1.24	8.94
10	10 cm	6.06	2.63	1.21	8.52
11	10 cm	8.63	3.06	1.34	9.03
12	10 cm	8.24	2.99	1.35	8.74
13	10 cm	7.57	2.84	1.25	8.82
14	10 cm	7.45	2.78	1.23	8.72
15	10 cm	7.05	3.64	1.26	8.41
16	10 cm	8.40	2.97	1.29	8.97
17	10 cm	7.07	2.78	1.29	9.10
18	10 cm	8.22	2.96	1.30	8.79
19	10 cm	9.60	3.27	1.37	8.92
20	10 cm	8.03	2.99	1.31	8.77
21	10 cm	7.90	2.97	1.32	9.01
22	10 cm	7.80	2.94	1.32	8.88

(continued on next page)

Appendix B (continued)

Day	Location	Acetate (mM)	Cl (mM)	Br (mM)	SO ₄ (mM)
23	10 cm	7.52	2.88	1.29	9.27
24	10 cm	7.27	2.81	1.31	8.98
25	10 cm	7.27	2.81	1.21	8.95
26	10 cm	7.05	2.77	1.21	8.87
27	10 cm	6.97	2.79	1.24	8.94
28	10 cm	6.76	2.75	1.26	8.85
29	10 cm	7.98	2.91	1.28	8.72
30	10 cm	6.46	2.69	1.18	8.73
31	10 cm	6.88	2.86	1.25	8.92
32	10 cm	6.48	2.78	1.25	8.56
33	10 cm	8.29	3.00	1.28	9.95
34	10 cm	7.83	2.95	1.31	8.27
35	10 cm	7.29	2.88	1.28	8.11
36	10 cm	8.03	2.89	1.24	7.91
37	10 cm	7.70	3.08	1.32	7.63
38	10 cm	6.26	2.85	1.24	7.32
39	10 cm	5.72	2.90	1.27	7.12
40	10 cm	5.45	2.97	1.22	6.71
41	10 cm	6.21	3.04	1.30	7.05
42	10 cm	5.31	2.95	1.24	6.42
43	10 cm	5.55	3.03	1.30	6.60
1	30 cm	0.00	2.95	0.63	9.01
2	30 cm	5.58	2.90	1.07	9.02
3	30 cm	8.49	3.14	1.48	9.02
4	30 cm	6.60	2.80	1.29	8.89
5	30 cm	7.14	2.94	1.27	8.95
6	30 cm	7.07	2.90	1.26	8.70
7	30 cm	8.81	3.18	1.30	8.96
8	30 cm	7.31	2.90	1.24	8.91
9	30 cm	6.27	2.68	1.22	8.90
10	30 cm	6.39	2.69	1.23	9.27
11	30 cm	7.48	2.85	1.28	8.22
12	30 cm	8.18	3.02	1.33	8.73
13	30 cm	7.55	2.89	1.27	8.90
14	30 cm	7.28	2.76	1.23	8.63
15	30 cm	8.31	3.02	1.30	8.93
16	30 cm	7.97	2.96	1.28	8.65
17	30 cm	8.30	3.03	1.34	9.04
18	30 cm	8.11	3.00	1.32	8.82
19	30 cm	8.13	3.23	1.33	8.97
20	30 cm	8.06	3.05	1.31	8.85
21	30 cm	9.24	3.23	1.37	9.02
22	30 cm	7.72	2.94	1.31	8.82
23	30 cm	7.49	2.89	1.30	9.28
24	30 cm	7.16	2.83	1.27	8.97
25	30 cm	7.05	2.80	1.22	8.85
26	30 cm	8.27	3.04	1.27	8.78
27	30 cm	7.26	2.98	1.32	8.99
28	30 cm	6.34	2.76	1.26	8.69
29	30 cm	5.97	2.67	1.21	8.60
30	30 cm	5.98	2.69	1.19	8.40
31	30 cm	6.16	2.83	1.26	8.54
32	30 cm	5.60	2.78	1.30	8.03
33	30 cm	7.45	2.99	1.31	8.49
34	30 cm	6.37	3.01	1.27	7.02
35	30 cm	5.37	2.93	1.24	6.99
36	30 cm	5.73	2.89	1.24	6.53
37	30 cm	4.92	3.00	1.27	5.20
38	30 cm	4.03	2.88	1.24	4.54
39	30 cm	2.14	2.95	1.26	4.15

Appendix B (continued)

Day	Location	Acetate (mM)	Cl (mM)	Br (mM)	SO ₄ (mM)
40	30 cm	2.87	2.81	1.22	3.83
41	30 cm	3.09	3.04	1.28	3.65
42	30 cm	2.36	2.99	1.24	3.40
43	30 cm	2.48	3.05	1.29	3.30
1	50 cm	0.00	3.00	0.00	9.05
2	50 cm	0.00	2.92	0.72	8.94
3	50 cm	6.12	2.88	1.18	8.97
4	50 cm	6.63	2.85	1.27	9.01
5	50 cm	6.93	2.97	1.28	9.01
6	50 cm	6.71	2.97	1.26	8.94
7	50 cm	6.77	2.93	1.25	9.00
8	50 cm	8.24	3.14	1.28	8.85
9	50 cm	6.10	2.72	1.22	8.99
10	50 cm	5.94	2.63	1.21	8.74
11	50 cm	8.17	3.06	1.35	8.97
12	50 cm	7.93	3.00	1.32	8.72
13	50 cm	7.33	2.88	1.26	8.84
14	50 cm	7.13	2.78	1.25	8.66
15	50 cm	6.62	2.76	1.26	8.79
16	50 cm	7.56	2.97	1.30	8.64
17	50 cm	8.14	3.03	1.34	9.01
18	50 cm	6.47	2.72	1.27	8.89
19	50 cm	8.05	3.05	1.41	8.97
20	50 cm	9.33	3.25	1.42	8.80
21	50 cm	7.83	3.00	1.33	9.04
22	50 cm	7.59	2.93	1.31	8.76
23	50 cm	7.25	2.89	1.30	9.27
24	50 cm	8.25	3.07	1.33	8.92
25	50 cm	6.85	2.81	1.21	8.75
26	50 cm	7.98	3.02	1.29	8.67
27	50 cm	6.30	2.80	1.25	8.73
28	50 cm	7.48	3.02	1.30	8.47
29	50 cm	5.65	2.68	1.22	8.36
30	50 cm	5.43	2.69	1.19	8.13
31	50 cm	5.55	2.95	1.26	8.14
32	50 cm	6.28	3.06	1.31	7.82
33	50 cm	5.70	2.94	1.32	6.88
34	50 cm	5.75	3.05	1.25	6.25
35	50 cm	5.23	2.90	1.24	5.61
36	50 cm	4.07	2.91	1.24	6.01
37	50 cm	3.00	2.92	1.27	3.86
38	50 cm	1.42	2.88	1.24	2.76
39	50 cm	0.37	2.94	1.25	2.27
40	50 cm	0.00	2.85	1.23	1.75
41	50 cm	0.08	3.14	1.27	1.48
42	50 cm	0.00	3.02	1.24	1.32
43	50 cm	0.00	3.13	1.27	1.29
1	70 cm	0.00	2.96	0.00	9.09
2	70 cm	0.00	2.94	0.55	8.94
3	70 cm	4.56	2.92	1.08	9.08
4	70 cm	6.46	2.88	1.24	9.04
5	70 cm	6.55	2.99	1.28	9.11
6	70 cm	7.40	3.19	1.34	8.85
7	70 cm	7.78	3.17	1.29	9.01
8	70 cm	6.39	2.84	1.23	8.75
9	70 cm	5.94	2.70	1.22	8.93
10	70 cm	5.65	2.62	1.21	8.59
11	70 cm	7.98	3.07	1.33	8.92
12	70 cm	7.83	2.97	1.32	8.71

(continued on next page)

Appendix B (continued)

Day	Location	Acetate (mM)	Cl (mM)	Br (mM)	SO ₄ (mM)
13	70 cm	8.57	3.10	1.30	8.86
14	70 cm	7.08	2.79	1.24	8.74
15	70 cm	8.00	3.00	1.33	8.86
16	70 cm	7.79	2.98	1.29	8.77
17	70 cm	8.03	3.02	1.33	9.09
18	70 cm	7.81	2.97	1.32	8.87
19	70 cm	7.96	3.06	1.33	9.00
20	70 cm	7.88	3.02	1.32	8.80
21	70 cm	9.14	3.25	1.38	9.13
22	70 cm	7.45	2.94	1.31	8.72
23	70 cm	8.50	3.12	1.34	9.15
24	70 cm	8.37	3.11	1.35	8.95
25	70 cm	6.70	2.83	1.22	8.74
26	70 cm	6.49	2.79	1.22	8.62
27	70 cm	6.05	2.80	1.25	8.54
28	70 cm	5.85	2.78	1.31	8.29
29	70 cm	5.44	2.72	1.24	8.16
30	70 cm	5.05	2.70	1.24	7.78
31	70 cm	5.22	2.95	1.29	8.01
32	70 cm	4.20	2.80	1.25	7.10
33	70 cm	5.41	3.04	1.31	6.49
34	70 cm	4.94	2.94	1.26	5.35
35	70 cm	3.81	2.88	1.23	4.70
36	70 cm	2.74	2.91	1.25	4.00
37	70 cm	1.41	3.00	1.27	2.72
38	70 cm	0.00	2.97	1.24	1.66
39	70 cm	0.00	2.96	1.25	1.21
40	70 cm	0.00	2.93	1.22	0.87
41	70 cm	0.00	3.13	1.27	0.59
42	70 cm	0.00	3.07	1.24	0.57
43	70 cm	0.00	3.17	1.27	0.59
1	90 cm	0.00	2.90	0.00	9.09
2	90 cm	0.00	3.05	0.48	8.94
3	90 cm	2.29	2.94	0.92	9.04
4	90 cm	5.58	2.93	1.17	9.02
5	90 cm	6.30	3.01	1.25	9.09
6	90 cm	5.46	2.94	1.25	8.84
7	90 cm	7.31	3.17	1.34	9.06
8	90 cm	6.11	2.88	1.24	8.86
9	90 cm	6.98	3.00	1.26	8.95
10	90 cm	5.28	2.64	1.20	8.65
12	90 cm	7.69	3.01	1.32	8.80
13	90 cm	7.10	2.85	1.26	8.93
14	90 cm	6.87	2.78	1.24	8.72
15	90 cm	7.86	3.04	1.34	8.87
16	90 cm	7.72	2.98	1.32	8.73
17	90 cm	7.90	3.03	1.33	9.07
18	90 cm	6.36	2.73	1.26	8.84
19	90 cm	7.98	3.08	1.34	9.02
20	90 cm	7.78	3.03	1.33	8.81
21	90 cm	7.58	3.00	1.32	8.99
22	90 cm	7.30	2.94	1.30	8.71
23	90 cm	8.28	3.12	1.33	9.07
24	90 cm	6.95	2.88	1.29	9.00
25	90 cm	7.97	3.06	1.26	8.65
26	90 cm	6.40	2.82	1.22	8.58
27	90 cm	5.88	2.82	1.31	8.48
28	90 cm	5.57	2.80	1.26	8.11

Appendix B (continued)

Day	Location	Acetate (mM)	Cl (mM)	Br (mM)	SO ₄ (mM)
29	90 cm	4.96	2.71	1.20	7.83
30	90 cm	4.40	2.69	1.25	7.45
31	90 cm	4.28	2.88	1.27	7.27
32	90 cm	3.34	2.81	1.28	6.44
33	90 cm	5.35	3.04	1.31	5.79
34	90 cm	4.03	2.98	1.28	4.76
35	90 cm	3.16	3.08	1.25	4.48
36	90 cm	1.71	2.93	1.24	3.31
37	90 cm	0.59	2.99	1.27	2.19
38	90 cm	0.00	3.00	1.25	1.25
39	90 cm	0.00	3.00	1.26	0.80
40	90 cm	0.00	2.96	1.23	0.69
41	90 cm	0.00	3.08	1.28	0.49
42	90 cm	0.00	3.01	1.25	0.47
43	90 cm	0.00	3.16	1.27	0.48
1	Effluent	0.00	2.78	0.00	8.63
2	Effluent	0.00	3.06	0.50	8.79
3	Effluent	0.86	3.00	0.77	8.91
4	Effluent	4.58	3.10	1.04	8.67
5	Effluent	6.25	3.01	1.23	9.09
6	Effluent	6.13	3.12	1.33	8.62
7	Effluent	5.54	2.92	1.28	9.05
8	Effluent	7.04	3.09	1.32	8.76
9	Effluent	5.07	2.69	1.21	8.80
10	Effluent	6.73	2.88	1.26	8.75
11	Effluent	8.08	3.05	1.34	9.09
12	Effluent	7.56	3.04	1.33	8.79
13	Effluent	8.04	3.04	1.30	8.75
14	Effluent	6.85	2.84	1.26	8.83
15	Effluent	7.52	2.99	1.32	8.81
16	Effluent	7.42	2.95	1.31	8.63
17	Effluent	6.37	2.81	1.29	9.01
19	Effluent	7.80	3.05	1.33	8.97
20	Effluent	8.85	3.24	1.38	8.63
21	Effluent	7.31	2.94	1.31	8.73
22	Effluent	8.51	3.14	1.38	8.66
23	Effluent	8.13	3.07	1.34	8.97
24	Effluent	6.74	2.86	1.29	9.02
25	Effluent	6.62	2.86	1.22	8.71
26	Effluent	6.20	2.82	1.23	8.53
27	Effluent	5.74	2.79	1.30	8.26
28	Effluent	5.34	2.81	1.27	7.99
29	Effluent	4.44	2.65	1.18	7.57
30	Effluent	5.06	2.95	1.24	7.17
31	Effluent	3.74	2.90	1.27	6.96
32	Effluent	2.68	2.80	1.24	6.00
33	Effluent	4.63	3.01	1.26	5.40
34	Effluent	3.52	2.97	1.26	4.28
35	Effluent	1.88	2.96	1.24	3.59
36	Effluent	0.94	2.93	1.25	2.85
37	Effluent	0.00	2.92	1.27	1.92
38	Effluent	0.00	2.99	1.24	1.22
39	Effluent	0.00	2.97	1.25	0.78
40	Effluent	0.00	2.87	1.22	0.70
41	Effluent	0.00	3.08	1.27	0.53
42	Effluent	0.00	3.01	1.25	0.49
43	Effluent	0.00	3.05	1.26	0.47

APPENDIX C

Aqueous ferrous iron, sulfide and pH in column effluent

Day	Fe ⁺⁺ (μM)	HS ⁻ (μM)	pH
1	3.22	0.69	7.21
2	4.30	0.28	7.23
3	2.51	0.12	7.25
4	2.51	0.03	7.24
5	9.31	0.16	7.24
6	22.38	0.22	7.27
7	33.49	0.34	7.21
8	37.25	0.28	7.25
9	46.02	0.00	7.14
10	46.92	0.06	7.3
11	51.57	0.00	7.31
12	53.36	0.09	7.27
13	57.84	0.00	7.3
14	61.60	0.12	7.32
15	66.61	0.16	7.3
16	74.49	0.12	7.32
17	75.21	0.28	7.27
18	81.65	0.31	7.3
19	82.37	0.78	7.32
20	83.45	1.09	7.39
21			7.31
22	84.88	2.31	7.39
23	92.94	3.80	7.41
24	93.83	4.86	7.38
25	93.11	6.05	7.41
26	91.32	10.10	7.42
27	71.63	8.76	7.44
28	79.51	10.16	7.45
29	79.15	9.60	7.47
30	69.48	12.22	7.57
31	56.59	3.40	7.53
32	47.09	6.89	
33	34.38	8.67	7.57
34	24.17	14.03	7.63
35	16.83	26.49	7.67
36	10.92	29.46	7.7
37	12.00	35.43	7.74
38	9.85	24.47	7.75
39	10.21	25.09	7.76
40	13.25	6.55	7.85
41	20.41	1.46	7.8
42	22.92	0.56	7.84
43	18.09	1.37	7.86

APPENDIX D

δ³⁴S of SO₄²⁻ and HS⁻

Day	Location	δ ³⁴ S SO ₄ (‰)
1	10 cm	6.38
2	10 cm	
3	10 cm	6.27
4	10 cm	6.23
5	10 cm	6.23
6	10 cm	
7	10 cm	6.36

Appendix D (continued)

Day	Location	δ ³⁴ S SO ₄ (‰)
8	10 cm	6.35
9	10 cm	6.42
10	10 cm	6.29
11	10 cm	6.34
12	10 cm	6.40
13	10 cm	6.40
14	10 cm	6.40
15	10 cm	
16	10 cm	6.33
17	10 cm	6.33
18	10 cm	
19	10 cm	6.36
20	10 cm	6.50
21	10 cm	6.34
22	10 cm	6.53
23	10 cm	6.38
24	10 cm	6.55
25	10 cm	6.66
26	10 cm	6.78
27	10 cm	6.69
28	10 cm	6.81
29	10 cm	6.62
30	10 cm	6.85
31	10 cm	7.04
32	10 cm	7.08
33	10 cm	7.46
34	10 cm	7.62
35	10 cm	7.76
36	10 cm	8.03
37	10 cm	8.76
38	10 cm	8.84
39	10 cm	9.36
41	10 cm	9.64
42	10 cm	9.93
43	10 cm	10.31
1	30 cm	6.28
2	30 cm	
3	30 cm	6.32
4	30 cm	6.30
5	30 cm	6.31
6	30 cm	6.42
7	30 cm	6.39
8	30 cm	6.40
9	30 cm	6.49
10	30 cm	6.24
11	30 cm	6.34
12	30 cm	6.41
13	30 cm	6.42
14	30 cm	6.44
15	30 cm	
16	30 cm	6.34
17	30 cm	6.37
18	30 cm	
19	30 cm	6.34
20	30 cm	6.38
21	30 cm	6.44
22	30 cm	6.72
23	30 cm	6.60
24	30 cm	6.70
25	30 cm	6.69

(continued on next page)

Appendix D (*continued*)

Day	Location	$\delta^{34}\text{S SO}_4$ (‰)
26	30 cm	6.81
27	30 cm	6.80
28	30 cm	6.98
29	30 cm	6.98
30	30 cm	7.13
31	30 cm	7.49
32	30 cm	7.84
33	30 cm	8.46
34	30 cm	9.23
35	30 cm	9.65
36	30 cm	10.55
37	30 cm	11.68
38	30 cm	13.31
39	30 cm	14.18
40	30 cm	15.46
41	30 cm	15.72
42	30 cm	16.69
43	30 cm	17.18
1	50 cm	6.34
2	50 cm	
3	50 cm	6.35
4	50 cm	6.29
5	50 cm	6.35
6	50 cm	6.31
7	50 cm	6.27
8	50 cm	6.31
9	50 cm	6.35
10	50 cm	6.43
11	50 cm	6.31
12	50 cm	6.29
14	50 cm	6.33
15	50 cm	
16	50 cm	6.32
17	50 cm	6.39
18	50 cm	6.36
19	50 cm	6.40
20	50 cm	6.41
21	50 cm	6.67
22	50 cm	6.72
23	50 cm	6.75
24	50 cm	6.68
25	50 cm	6.67
26	50 cm	6.94
27	50 cm	6.94
28	50 cm	7.18
29	50 cm	7.27
30	50 cm	7.59
31	50 cm	7.84
32	50 cm	8.36
33	50 cm	9.26
34	50 cm	10.36
35	50 cm	11.03
36	50 cm	12.64
37	50 cm	14.79
38	50 cm	18.00
39	50 cm	19.75
40	50 cm	22.59
41	50 cm	24.73
42	50 cm	25.49
43	50 cm	27.42

Appendix D (*continued*)

Day	Location	$\delta^{34}\text{S SO}_4$ (‰)
1	70 cm	6.24
2	70 cm	
3	70 cm	6.33
4	70 cm	6.24
5	70 cm	6.29
6	70 cm	6.38
7	70 cm	6.33
8	70 cm	6.32
9	70 cm	6.41
10	70 cm	6.36
11	70 cm	6.33
12	70 cm	6.39
13	70 cm	6.26
14	70 cm	6.24
15	70 cm	
16	70 cm	6.26
17	70 cm	6.38
18	70 cm	
19	70 cm	
20	70 cm	6.36
21	70 cm	6.56
22	70 cm	6.60
23	70 cm	6.61
24	70 cm	6.68
25	70 cm	6.82
26	70 cm	6.98
27	70 cm	7.04
28	70 cm	7.35
29	70 cm	7.46
30	70 cm	7.75
31	70 cm	8.31
32	70 cm	8.93
33	70 cm	10.20
34	70 cm	11.64
35	70 cm	12.64
36	70 cm	14.97
37	70 cm	18.16
38	70 cm	23.47
39	70 cm	26.82
40	70 cm	31.43
41	70 cm	37.39
42	70 cm	37.44
43	70 cm	39.59
1	90 cm	6.25
2	90 cm	
3	90 cm	6.21
4	90 cm	6.32
5	90 cm	6.46
6	90 cm	6.24
7	90 cm	6.47
8	90 cm	6.32
9	90 cm	6.33
10	90 cm	6.40
11	90 cm	6.26
12	90 cm	6.39
13	90 cm	6.35
14	90 cm	6.46
15	90 cm	
16	90 cm	6.38
17	90 cm	6.37

(continued on next page)

Appendix D (continued)

Day	Location	$\delta^{34}\text{S SO}_4$ (‰)	
18	90 cm		
19	90 cm		
20	90 cm	6.48	
21	90 cm	6.66	
22	90 cm	6.87	
23	90 cm	6.68	
24	90 cm	6.84	
25	90 cm	6.90	
26	90 cm	7.10	
27	90 cm	7.34	
28	90 cm	7.63	
29	90 cm	7.90	
30	90 cm	8.14	
31	90 cm	8.96	
32	90 cm	9.96	
33	90 cm	10.84	
34	90 cm	12.87	
35	90 cm	13.82	
36	90 cm	16.60	
37	90 cm	20.27	
38	90 cm	26.89	
39	91 cm	30.82	
40	90 cm	35.71	
41	90 cm	38.90	
42	90 cm	39.59	
43	90 cm	42.32	
1	Effluent	6.33	
2	Effluent		
3	Effluent		
4	Effluent	6.36	
5	Effluent	6.29	
6	Effluent	6.37	
7	Effluent	6.38	
8	Effluent	6.44	
9	Effluent		
10	Effluent		
11	Effluent		
12	Effluent		
13	Effluent		
14	Effluent		
15	Effluent		
16	Effluent	6.23	
17	Effluent	6.42	
18	Effluent	6.35	
19	Effluent		
20	Effluent	6.42	
21	Effluent	6.56	
Day	Location	$\delta^{34}\text{S SO}_4$ (‰)	$\delta^{34}\text{S HS}^-$ (‰)
22	Effluent	6.53	
23	Effluent	6.53	−3.42
24	Effluent	6.78	
25	Effluent	6.97	
26	Effluent	7.19	−4.28
27	Effluent	7.33	−4.26
28	Effluent	7.62	−4.23
29	Effluent		
30	Effluent	8.69	
31	Effluent	9.24	−2.22
32	Effluent	10.24	
33	Effluent	11.29	−0.88

Appendix D (continued)

Day	Location	$\delta^{34}\text{S SO}_4$ (‰)	$\delta^{34}\text{S HS}^-$ (‰)
34	Effluent	12.91	−0.58
35	Effluent	14.91	1.59
36	Effluent	17.14	4.23
37	Effluent	21.37	6.67
38	Effluent	26.40	10.24
39	Effluent	29.76	11.44
40	Effluent	32.56	8.94
41	Effluent	35.91	
42	Effluent	35.32	
43	Effluent	36.32	

APPENDIX E

Modeled secondary species and associated equilibrium constants

Speciation reaction	$\log K_{\text{eq}}$
$\text{H}_2\text{O} \leftrightarrow \text{H}^+ + \text{OH}^-$	−14.0
$\text{HCO}_3^- + \text{H}^+ \leftrightarrow \text{CO}_{2(\text{aq})} + \text{H}_2\text{O}$	6.34
$\text{CO}_3^{2-} + 2\text{H}^+ \leftrightarrow \text{CO}_{2(\text{aq})} + \text{H}_2\text{O}$	16.7
$\text{FeOH}^+ + \text{H}^+ \leftrightarrow \text{Fe}^{2+} + \text{H}_2\text{O}$	9.5
$\text{Fe}(\text{OH})_{2(\text{aq})} + 2\text{H}^+ \leftrightarrow \text{Fe}^{2+} + \text{H}_2\text{O}$	20.6
$\text{Fe}(\text{OH})_3 + 3\text{H}^+ \leftrightarrow \text{Fe}^{2+} + 3\text{H}_2\text{O}$	31.0
$\text{FeOH}^{2+} + \text{H}^+ \leftrightarrow \text{Fe}^{3+} + \text{H}_2\text{O}$	2.19
$\text{FeCl}^+ \leftrightarrow \text{Fe}^{2+} + \text{Cl}^-$	0.165
$\text{FeCl}^{2+} \leftrightarrow \text{Fe}^{3+} + \text{Cl}^-$	0.815
$\text{Fe}(\text{OH})_2 + 2\text{H}^+ \leftrightarrow \text{Fe}^{3+} + 2\text{H}_2\text{O}$	5.67
$\text{Fe}(\text{OH})_{3(\text{aq})} + 3\text{H}^+ \leftrightarrow \text{Fe}^{3+} + 3\text{H}_2\text{O}$	12.0
$\text{Fe}^{32}\text{S}_{(\text{aq})} + 2\text{H}^+ \leftrightarrow \text{Fe}^{2+} + \text{H}_2^{32}\text{S}_{(\text{aq})}$	9.2
$\text{Fe}^{34}\text{S}_{(\text{aq})} + 2\text{H}^+ \leftrightarrow \text{Fe}^{2+} + \text{H}_2^{34}\text{S}_{(\text{aq})}$	9.2
$\text{FeCO}_{3(\text{aq})} + 2\text{H}^+ \leftrightarrow \text{Fe}^{2+} + \text{CO}_{2(\text{aq})} + \text{H}_2\text{O}$	11.9
$\text{Fe}(\text{CH}_3\text{COO})_{2(\text{aq})} \leftrightarrow \text{Fe}^{2+} + 2\text{CH}_3\text{COO}^-$	−2.48
$\text{FeCH}_3\text{COO}^- \leftrightarrow \text{Fe}^{2+} + \text{CH}_3\text{COO}^-$	−1.29
$\text{CaOH}^+ + \text{H}^+ \leftrightarrow \text{Ca}^{2+} + \text{H}_2\text{O}$	12.9
$\text{CaCO}_{3(\text{aq})} + 2\text{H}^+ \leftrightarrow \text{Ca}^{2+} + \text{H}_2\text{O} + \text{CO}_{2(\text{aq})}$	13.4
$\text{Ca}^{32}\text{SO}_{4(\text{aq})} \leftrightarrow \text{Ca}^{2+} + {}^{32}\text{SO}_4^{2-}$	−2.1
$\text{Ca}^{34}\text{SO}_{4(\text{aq})} \leftrightarrow \text{Ca}^{2+} + {}^{34}\text{SO}_4^{2-}$	−2.1
$\text{CaCl}^- \leftrightarrow \text{Ca}^{2+} + \text{Cl}^-$	0.7
$\text{CaHCO}_3^+ + \text{H}^+ \leftrightarrow \text{Ca}^{2+} + \text{H}_2\text{O} + \text{CO}_{2(\text{aq})}$	5.3
$\text{Ca}(\text{CH}_3\text{COO})_{2(\text{aq})} \leftrightarrow \text{Ca}^{2+} + \text{CH}_3\text{COO}^-$	−2.13
$\text{Ca}(\text{CH}_3\text{COO})^+ \leftrightarrow \text{Ca}^{2+} + \text{CH}_3\text{COO}^-$	−0.928
$\text{MgCO}_{3(\text{aq})} + 2\text{H}^+ \leftrightarrow \text{Mg}^{2+} + \text{H}_2\text{O} + \text{CO}_{2(\text{aq})}$	13.7
$\text{MgCl}^- \leftrightarrow \text{Mg}^{2+} + \text{Cl}^-$	0.139
$\text{Mg}^{32}\text{SO}_{4(\text{aq})} \leftrightarrow \text{Mg}^{2+} + {}^{32}\text{SO}_4^{2-}$	−2.41
$\text{Mg}^{34}\text{SO}_{4(\text{aq})} \leftrightarrow \text{Mg}^{2+} + {}^{34}\text{SO}_4^{2-}$	−2.41
$\text{CH}_3\text{COOH}_{(\text{aq})} \leftrightarrow \text{H}^+ + \text{CH}_3\text{COO}^-$	−4.75
$\text{H}^{32}\text{S}^- + \text{H}^+ \leftrightarrow \text{H}_2^{32}\text{S}_{(\text{aq})}$	6.98
$\text{H}^{34}\text{S}^- + \text{H}^+ \leftrightarrow \text{H}_2^{34}\text{S}_{(\text{aq})}$	6.98
${}^{32}\text{S}^{2-} + 2\text{H}^+ \leftrightarrow \text{H}_2^{32}\text{S}_{(\text{aq})}$	19.9
${}^{34}\text{S}^{2-} + 2\text{H}^+ \leftrightarrow \text{H}_2^{34}\text{S}_{(\text{aq})}$	19.9
$\text{NH}_{3(\text{aq})} + \text{H}^+ \leftrightarrow \text{NH}_4^+$	9.24

REFERENCES

- Anderson R. T., Vrionis H. A., Ortiz-Bernad I., Resch C. T., Long P. E., Dayvault R., Karp K., Marutzky S., Metzler D. R., Peacock A., White D. C., Lowe M. and Lovely D. R. (2003) Stimulating the *in situ* activity of *Geobacter* species to remove

- uranium from the groundwater of a uranium-contaminated aquifer. *Appl. Environ. Microbiol.* **69**, 5884–5891.
- Bargar J. R., Williams K. H., Campbell K. M., Long P. E., Stubbs J. E., Suvorava E., Lexama-Pacheco J., Alessi D. S., Stylo M., Webb S. M., Davis J. A., Giammar D. E., Blue L. Y. and Bernier-Latmani R. (2013) Uranium redox transition pathways in acetate – amended sediments. *Proc. Nat. Acad. Sci.* **110**(12), 4506–4511.
- Benner S. G., Blowes D. W., Gould W. D., Herbert R. B. and Ptacek C. J. (1999) Geochemistry of a permeable reactive barrier for metals and acid mine drainage. *Environ. Sci. Technol.* **33**(16), 2793–2799.
- Brunner B. and Bernasconi S. M. (2005) A revised isotope fractionation model for dissimilatory sulfate reduction in sulfate reducing bacteria. *Geochim. Cosmochim. Acta* **69**, 4759–4771.
- Burris D. R., Hatfield K. and Wolfe N. L. (1996) Laboratory experiments with heterogeneous reactions in mixed porous media. *J. Environ. Eng.* **122**, 685–691.
- Canfield D. E., Olsen C. A. and Cox R. P. (2006) Temperature and its control of isotope fractionation by sulfate-reducing bacterium. *Geochim. Cosmochim. Acta* **70**, 548–561.
- Canfield D. E. (2001) Isotope fractionation by natural populations of sulfate-reducing bacteria. *Geochim. Cosmochim. Acta* **65**, 1117–1124.
- Dale A. W., Brüchert V., Alperin M. and Regnier P. (2009) An integrated sulfur isotope model for Namibian shelf sediments. *Geochim. Cosmochim. Acta* **73**, 1924–1944.
- Dale A. W., Regnier P., Knab N. J., Jørgensen B. B. and Van Cappellen P. (2008) Anaerobic oxidation of methane (AOM) in marine sediments from the Skagerrak (Denmark): II, Reaction-transport modeling. *Geochim. Cosmochim. Acta* **72**, 2880–2894.
- Detmers J., Brüchert V., Habicht K. S. and Luever J. (2001) Diversity of sulfur isotope fractionations by sulfate-reducing prokaryotes. *Appl. Environ. Microbiol.* **67**, 888–894.
- DePaolo D. J. (2011) Surface kinetic model for isotopic and trace element fractionation during precipitation of calcite from aqueous solutions. *Geochim. Cosmochim. Acta* **75**, 1039–1056.
- DOE (2011) Review of the Natural Flushing Groundwater Remedy at the Old Rifle Legacy Management Site, Rifle, Colorado (Draft). DOE/LMS-S07263, Grand Junction Office, Grand Junction, Colorado.
- DOE (1999) Final Site Observational Work Plan for the UMTRA Project Old Rifle Site, GJO-99-88-TAR, Rev. 1, Grand Junction Office, Grand Junction, Colorado.
- Druhan J. L., Conrad M. E., Bill M., Lim H. C., Wu C., Williams K. H., DePaolo D. J. and Brodie E. L. (2014) A large column analog experiment of stable isotope variations during reactive transport: II. Carbon mass balance, microbial community structure and predation. *Geochim. Cosmochim. Acta* **124**, 394–409.
- Druhan J. L., Steefel C. I., Williams K. H. and DePaolo D. J. (2013) Calcium isotope fractionation in groundwater: molecular scale processes influencing field scale behavior. *Geochim. Cosmochim. Acta* **119**, 93–116.
- Druhan J. L., Steefel C. I., Molins S., Williams K. H., Conrad M. E. and DePaolo D. J. (2012) Timing the onset of sulfate reduction over multiple subsurface acetate amendments by measurement and modeling of sulfur isotope fractionation. *Environ. Sci. Technol.* **46**(16), 8895–8902.
- Druhan J. L., Conrad M. E., Williams K. E., N'Guessan L., Long P. E. and Hubbard S. S. (2008) Sulfur isotopes as indicators of amended bacterial sulfate reduction processes influencing field scale uranium bioremediation. *Environ. Sci. Technol.* **42**, 7842–7849.
- Fand R. M. and Thinakaran R. (1990) The influence of the wall on flow through pipes packed with spheres. *J. Fluids Eng., Trans. ASME* **112**, 84–88.
- Fang Y. L., Yabusaki S. B., Morrison S. J., Amonette J. P. and Long P. E. (2009) Multicomponent reactive transport modeling of uranium bioremediation field experiments. *Geochim. Cosmochim. Acta* **73**, 6029–6051.
- Farquhar J., Johnston D. T., Wing B. A., Habicht K. S., Canfield D. E., Airieau S. A. and Thiemens M. H. (2003) Multiple sulfur isotopic interpretations of biosynthetic pathways: implications for biological signatures in the sulfur isotope record. *Geobiology* **1**, 15–27.
- Freeze A. R. and Cherry J. A. (1979) *Groundwater*. Prentice Hall Inc. 604 p.
- Giambalyo E. R., Steefel C. I., Fisher A. T., Rosenberg N. D. and Wheat C. G. (2002) Effect of fluid-sediment reaction on hydrothermal fluxes of major elements, eastern flank of the Juan de Fuca Ridge. *Geochim. Cosmochim. Acta* **66**, 1739–1757.
- Gibson B. D., Amos R. T. and Blowes D. W. (2011) ³⁴S/³²S fractionation during sulfate reduction in groundwater treatment systems: reactive transport modeling. *Environ. Sci. Technol.* **45**, 2863–2870.
- Habicht K. S., Salling L., Thamdrup B. and Canfield D. E. (2005) Effect of low sulfate concentrations on lactate oxidation and isotope fractionation during sulfate reduction by *Archaeoglobus fulgidus* strain Z. *Appl. Environ. Microbiol.* **71**, 3770–3777.
- Habicht K. S. and Canfield D. E. (2001) Isotope fractionation by sulfate-reducing natural populations and the isotopic composition of sulfide in marine sediments. *Geology* **29**, 555–558.
- Harrison A. G. and Thode H. G. (1958) Mechanism of bacterial reduction of sulphate from isotope fractionation studies. *Trans. Faraday Soc.* **54**, 84–96.
- Harrison A. G. and Thode H. G. (1957) The kinetic isotope effect in the chemical reduction of sulphate. *Trans. Faraday Soc.* **53**, 1648–1660.
- Holmes D. E., Finneran K. T., O'Neil R. A. and Lovley D. R. (2002) Enrichment of the members of the family Geobacteraceae associated with stimulation of dissimilatory metal reduction in uranium-contaminated aquifer sediments. *Appl. Environ. Microbiol.* **68**(5), 2300–2306.
- Hua B., Xu H., Terry J. and Deng B. (2006) Kinetics of uranium(VI) reduction by hydrogen sulfide in anoxic aqueous systems. *Environ. Sci. Tech.* **40**, 4666–4671.
- Ingvorsen K., Zehnder A. J. B. and Jørgensen B. B. (1984) Kinetics of sulfate and acetate uptake by *Desulfobacter postgatei*. *Appl. Environ. Microbiol.* **47**, 403–408.
- Jamieson-Hanes J. H., Amos R. T. and Blowes D. W. (2012) Reactive transport modeling of chromium isotope fractionation during Cr(VI) reduction. *Environ. Sci. Technol.* **46**(24), 13311–13316.
- Jin Q. and Bethke C. M. (2003) A new rate law describing microbial respiration. *Appl. Environ. Microbiol.* **69**, 2340–2348.
- Johnston D. T., Farquhar J., Wing B. A., Kaufman A. J., Canfield D. E. and Habicht K. S. (2005) Multiple sulfur isotope fractionations in biological systems: a case study with sulfate reducers and sulfur disproportionators. *Am. J. Sci.* **305**, 645–660.
- Jørgensen B. B. (1979) A theoretical model of stable sulfur isotope distribution in marine sediments. *Geochim. Cosmochim. Acta* **43**, 363–374.
- Jørgensen K. S. (2007) *In situ* bioremediation. *Adv. Appl. Microbiol.* **61**, 285–305.
- Kaplan I. R. and Rittenberg S. C. (1964) Microbial fractionation of sulfur isotopes. *Gen. Microbiol.* **43**, 195–212.
- Knöller K., Vogt C., Feisthauer S., Weise S. M. and Richnow H. H. (2008) Sulfur cycling and biodegradation in contaminated

- aquifers: insights from stable isotope investigations. *Environ. Sci. Technol.* **42**, 7807–7812.
- Knöller K., Vogt C., Richnow H. H. and Weise S. M. (2006) Sulfur and oxygen isotope fractionation during benzene, toluene, ethyl benzene and zylene degradation by sulfate-reducing bacteria. *Environ. Sci. Technol.* **40**, 3879–3885.
- Koch A. L. (1998) The Monod model and its alternatives. In *Mathematical Modeling in Microbial Ecology* (eds. A. L. Koch, J. A. Robinson and G. A. Milliken). Chapman & Hall, London.
- Komlos J., Moon H. S. and Jaffé P. R. (2008) Effect of sulfate on the simultaneous bioreduction of iron and uranium. *J. Environ. Qual.* **37**, 2058–2062.
- Gelhar L. W., Welty C. and Rehfeldt K. R. (1992) A critical-review of data on field-scale dispersion in aquifers. *Water Resour. Res.* **28**, 155–174.
- Li L., Gawande N., Kowalsky M. B., Steefel C. I. and Hubbard S. S. (2011) Physiochemical heterogeneity controls on uranium bioreduction rates at the field scale. *Environ. Sci. Technol.* **45**, 9959–9966.
- Li L., Steefel C. I., Kowalsky M. B., Englert A. and Hubbard S. S. (2010) Effects of physical and geochemical heterogeneities on mineral transformation and biomass accumulation during biostimulation experiments at Rifle, Colorado. *J. Contam. Hydrol.* **112**, 45–63.
- Li L., Steefel C. I., Williams K. H., Wilkins M. J. and Hubbard S. S. (2009) Mineral transformation and biomass accumulation associated with uranium bio-remediation at Rifle, Colorado. *Environ. Sci. Technol.* **43**, 5429–5435.
- Lovley, D. R. (ed.) (2000) *Environmental Microbe-Metal Interactions*. ASM Press, Washington, DC.
- Lovley D. R. and Phillips E. J. (1992) Reduction of uranium by *Desulfovibrio desulfuricans*. *Appl. Environ. Microbiol.* **58**(3), 850–856.
- Lovley D. R., Phillips E. J., Gorby Y. A. and Landa E. R. (1991) Microbial reduction of uranium. *Nature* **350**, 413–416.
- Maggi F. and Riley W. J. (2010) Mathematical treatment of isotopologue and isotopomer speciation and fractionation in biochemical kinetics. *Geochim. Cosmochim. Acta* **74**, 1823–1835.
- Maggi F. and Riley W. J. (2009) Transient competitive complexation in biological kinetic isotope fractionation explains non-steady isotopic effects: theory and application to denitrification of soils. *J. Geophys. Res. – Biogeosci.* **114**, G04012.
- Maher K., Steefel C. I., White A. F. and Stonestrom D. A. (2009) The role of reaction affinity and secondary minerals in regulating chemical weathering rates at the Santa Cruz Soil Chronosequence, California. *Geochim. Cosmochim. Acta* **73**, 2804–2831.
- Maher K., Steefel C. I., DePaolo D. J. and Viani B. (2006) The mineral dissolution rate conundrum: insights from reactive transport modeling of U isotopes and pore fluid chemistry in marine sediments. *Geochim. Cosmochim. Acta* **70**, 337–363.
- Mariotti A., Germon J. C., Hubert P., Kaiser P., Letolle R., Tardieux A. and Tardieux P. (1981) Experimental-determination of nitrogen kinetic isotope fractionation – some principles – illustration for the denitrification and nitrification processes. *Plant Soil* **62**, 413–430.
- Massmann G., Tichomirowa M., Merz C. and Pekdeger A. (2003) Sulfide oxidation and sulfate reduction in a shallow groundwater system (Oderbruch aquifer, Germany). *J. Hydrol.* **278**, 231–243.
- Michaelis L. and Menten M. M. (1913) Die kinetik der invertigwirkung (The kinetics of invertase activity). *Biochemische Zeitschrift* **49**, 333–369.
- Monod J. (1949) The growth of bacterial cultures. *Annu. Rev. Microbiol.* **3**, 371–394.
- Monod J. (1942) Recherches sur las croissance des culture bacteriennes (Research on the growth of bacterial cultures). Hermann et Cie.
- Moon H. S., McGuinness L., Kukkadapu R. K., Peacock A. D., Komlos J., Kerkhof L. J., Long P. E. and Jaffé P. R. (2010) Microbial reduction of uranium under iron- and sulfate-reducing conditions: effect of amended goethite on microbial community composition and dynamics. *Water Res.* **44**, 4015–4028.
- Moon H. S., Komlos J. and Jaffé P. R. (2009) Biogenic U(IV) oxidation by dissolution oxygen and nitrate in sediment after prolonged U(VI)/Fe(III)/SO₄²⁼ reduction. *J. Contam. Hydrol.* **105**, 18–27.
- Moon H. S., Komlos J. and Jaffé P. R. (2007) Uranium reoxidation in previously bioreduced sediment by dissolved oxygen and nitrate. *Environ. Sci. Technol.* **41**, 4587–4592.
- Navarre-Sitchler A., Steefel C. I., Sak P. B. and Brantley S. L. (2011) A reactive transport model for weathering rind formation on basalt. *Geochim. Cosmochim. Acta* **75**, 7644–7667.
- Rees C. E. (1973) A steady-state model for sulphur isotope fractionation in bacterial reduction processes. *Geochim. Cosmochim. Acta* **37**, 1141–1162.
- Rittmann B. E. and McCarty P. L. (2001) *Environmental Biotechnology: Principles and Applications*. McGraw-Hill, New York, NY, 754 p.
- Roden E. E. (2008) Microbiological controls on geochemical kinetics 1: fundamentals and case study on microbial Fe(III) oxide reduction. In *Kinetics of Water–Rock Interaction* (eds. S. L. Brantley, J. D. Kubicki and A. F. White). Springer, pp. 335–416.
- Sim M. S., Bosak T. and Ono S. (2011) Large sulfur isotope fractionation does not require disproportionation. *Science* **333**(6038), 74–77.
- Stam M. C., Mason P. R. D., Laverman A. M., Pallud C. and Van Cappellen P. (2011) (34)S/(32)S fractionation by sulfate-reducing microbial communities in estuarine sediments. *Geochim. Cosmochim. Acta* **75**, 3903–3914.
- Steefel C. I., Carroll S., Zhao P. H. and Roberts S. (2003) Cesium migration in Hanford sediment: a multiscale cation exchange model based on laboratory transport experiments. *J. Contam. Hydrol.* **67**, 219–246.
- Suzuki Y., Kelly S. D., Kemner K. M. and Banfield J. F. (2004) Enzymatic U(VI) reduction by *Desulfosporosinus* species. *Radiochim. Acta* **92**(1), 11–16.
- Thamdrup B., Fossing H. and Jorgensen B. B. (1994) Manganese, iron and sulfur cycling in a coastal marine sediment, Aarhus Bay, Denmark. *Geochim. Cosmochim. Acta* **58**(23), 5115–5129.
- Van Breukelen B. M. and Prommer H. (2008) Beyond the Rayleigh equation: reactive transport modeling of isotope fractionation effects to improve quantification of biodegradation. *Environ. Sci. Technol.* **42**, 2457–2463.
- Van Cappellen P. and Gaillard J. F. (1996) Biogeochemical dynamics in aquatic sediments. In *Reactive Transport in Porous Media*, vol. 34 (eds. P. C. Lichtner, C. I. Steefel and E. H. Oelkers). The Mineralogical Society of America, pp. 335–376.
- Vrionis H. A., Anderson R. T., Ortiz-Bernad I., O'Neill K. R., Resch C. T., Peacock A. D., Dayvault R., White D. C., Long P. E. and Lovley D. R. (2005) Microbiological and geochemical heterogeneity in an in situ uranium bioremediation field site. *Appl. Environ. Microbiol.* **71**, 6308–6318.
- Wehrmann L. M., Arndt S., März C., Ferdelman T. G. and Brunner B. (2013) The evolution of early diagenetic signals in Bering Sea seafloor sediments in response to varying organic carbon deposition over the last 4.3 Ma. *Geochim. Cosmochim. Acta* **109**, 175–196.

- Wersin P., Hochella M. F. Jr., Persson P., Redden G., Leckie J. O. and Harris D. W. (1994) Interaction between aqueous uranium (VI) and sulfide minerals: Spectroscopic evidence for sorption and reduction. *Geochim. Cosmochim. Acta* **58**(13), 2829–2843.
- White A. F., Bullen T. D., Vivit D. V., Schulz M. S. and Clow D. W. (1999) The role of disseminated calcite in the chemical weathering of granitoid rocks. *Geochim. Cosmochim. Acta* **63**, 1939–1953.
- Widerlund A., Nowell G. M., Davison W. and Pearson D. G. (2012) High-resolution measurements of sulphur isotope variations in sediment pore-waters by laser ablation multicollector inductively coupled plasma mass spectrometry. *Chem. Geol.* **291**, 278–285.
- Wijsman J. W. M., Middelburg J. J., Herman P. M. J., Böttcher M. E. and Heip C. H. R. (2001) Sulfur and iron speciation in surface sediments along the northwestern margin of the Black Sea. *Mar. Chem.* **74**(4), 261–278.
- Williams K. H., Long P. E., Davis J. A., Wilkins M. J., N'Guessan A. L., Steefel C. I., Yang L., Newcomer D., Spane F. A., Kerkhof L. J., McGuinness L., Dayvault R. and Lovely D. R. (2011) Acetate availability and its influence on sustainable bioremediation of uranium-contaminated groundwater. *Geomicrobiol. J.* **28**, 519–539.
- Yabusaki S. B., Fang Y., Williams K. H., Murray C. J., Ward A. L., Dayvault R. D., Waichler S. R., Newcomer D. R., Spane F. A. and Long P. E. (2011) Variably saturated flow and multicomponent biogeochemical reactive transport modeling of a uranium bioremediation field experiment. *J. Contam. Hydrol.* **126**, 271–290.

Associate editor: Jack J. Middelburg